Mixing of Two Scalars in Turbulent Channel Flow

Etienne Costa-Patry
Department of Mechanical Engineering
McGill University
Montréal, Québec, Canada

A thesis submitted to McGill University in partial fulfillment of the requirement of the degree of Master Engineering

Your file Votre référence
ISBN: 978-0-494-22640-7
Our file Notre référence
ISBN: 978-0-494-22640-7

Abstract

The interaction of two scalars (both temperature) emitted from concentrated line sources is studied in fully-developed, high-aspect-ratio, turbulent channel flow. The thermal fields are measured using cold-wire thermometry in a flow with a Reynolds number (Uh/v) of 10200.

The transverse, total RMS temperature profiles are a function of the separation distance between the line sources (d/h), their average wall-normal position (y_{s_av}/h), and the downstream location (x/h) (relative to the line sources). The non-dimensional form of the scalar covariance, the correlation coefficient (ρ), is a function of the same parameters and quantifies the mixing of the two scalars.

In all cases, the transverse profiles of the correlation coefficient flatten and tend towards 1 as x/h increases. The minimum value of the correlation coefficient for a given transverse profile (ρ_{min}) drifts towards the wall for line source combinations that are not symmetric about the channel centreline. (For profiles that are symmetric about the centreline, the minimum correlation coefficient always occurs at the centreline.) The initial downstream evolution of ρ_{min} (and $\rho_{ys\_av/h}$ – the value of the correlation coefficient measured at the average wall-normal source location) depend mostly on d/h. Therefore, to an extent, the measured evolutions are similar to those in homogeneous turbulence. However, the dependence on y_{s_av}/h is never entirely negligible. At a certain downstream position, the (inhomogeneous) high turbulence intensity (found near the wall) serves to accelerate the scalar mixing.

For line source combinations that are not influenced by the above-mentioned, near-wall, high turbulence intensities, spectral analysis indicates that the degree of mixing across scales is relatively constant for the range of parameters studied herein. In the case of near-wall mixing, the large scales were found to evolve more rapidly. This presumably derives from the large-scale nature of turbulence production, which is strong in the near-wall region.

Résumé

Les interactions entre deux scalaires (température) émis par des sources linéaires sont étudiées pour un écoulement turbulent et établi dans une soufflerie canalisée ayant un rapport hauteur-largeur élevé. Le nombre de Reynolds (Uh/v) de l'écoulement est de 10200.

Les profils transversaux de l'écart type de la température dépendent de la distance séparant les sources linéaires (d/h), de la position transversale moyenne (y_{s_av}/h) de ceux-ci, ainsi que la position en aval des sources linéaires (x/h). Le coefficient de corrélation (ρ), forme non-dimensionalisée de la covariance des scalaires, dépend des mêmes paramètres et quantifie le mélange des deux scalaires.

Les profils transversaux du coefficient de corrélation s'aplanissent et tendent vers l'unité dans leur évolution en x/h. Dans la direction transversale, le coefficient de corrélation minimum (ρ_{min}) se déplace vers le mur quand les sources ne se situent pas symétriquement autour de l'axe central de la soufflerie. Dans le cas des profils symétriques par rapport de l'axe central, le coefficient de corrélation minimum se retrouve toujours sur ce dernier. Il apparaît que ρ_{min} et $\rho_{ys\_av/h}$, le coefficient de corrélation mesuré à y_{s_av}/h, dépendent initialement majoritairement sur d/h. Dans ce cas, ils partagent des similitudes avec les évolutions observées en écoulement turbulent homogène. Il faut cependant noter que la dépendance sur y_{s_av}/h n'a pas pu être contournée et est constamment présente. À partir d'un certain point en aval des sources linéaires, le niveau élevé de turbulence près du mur accélère rapidement le mélange des scalaires.

L'analyse spectrale des interactions montre que les scalaires sont mélangés de façon égale à toutes les échelles lorsque les combinaisons de sources linéaires ne sont pas affectées par les niveaux élevés de turbulence près du mur. Pour les mesures faites à cet endroit, le mélange aux grandes échelles évolue rapidement. Ceci est possiblement dû à la production de la turbulence, importante près du mur et concentrée aux grandes échelles.

Acknowledgements

J'aimerais tout d'abord remercier le professeur Mydlarski pour son aide précieuse et ses encouragements généreux. Ils m'ont permis de me dépasser et m'ont transmis des valeurs et une éthique de travail auxquelles j'espère savoir faire honneur.

Mes remerciements s'étendent aussi à mon collègue Thomas Lavertu avec qui j'ai eu plaisir à travailler. Finalement, j'aimerais souligner le support de mes parents et amis et plus particulièrement de Claudia. À vous tous, merci.

Contents

List of figures

List of tables

1. Introduction

Fluid mechanics is a broad discipline of significant relevance to physics and engineering. Most electrical power is derived from fluid motion. Landscapes are created by water and air erosion. Fluid mechanics is a part of every life through breathing and blood flow.

Fluid flows are generally separated in three groups: laminar flows, transitional flows and turbulent flows. The latter is the most common in nature. The atmospheric boundary layer is turbulent as is the oceanic mixed layer and the flow of natural gas in pipelines.

The first description of turbulence can be tracked back to Leonardo da Vinci. Some of his drawings clearly show the complex nature of turbulence. The separation of fluid motion into laminar, transitional and turbulent regimes was described by Osborne Reynolds in late 1800s. Later, Sir G.I. Taylor pioneered the study of scalar turbulence. In 1913, he boarded the whaling ship Scotia for a meteorological survey of the coast of Newfoundland and Nova Scotia, where he became interested in the evolution of the plume of smoke coming from the steamer's furnace. In 1935, he published a theoretical study of turbulence, related to this phenomenon. Another Englishman, L.F. Richardson, was the first to describe the turbulent cascade in the early nineteen-twenties:

Big whirls have little whirls,
which feed on their velocity.
Little whirls have lesser whirls,
and so on to viscosity.[1]

An important advance in the understanding of the physics of turbulence was made when Kolmogorov, in 1941, predicted a spectral description of the turbulent cascade. He supposed that far enough into the cascade, eddies stopped being affected by the large-scale geometry and became locally isotropic. Since then, research has explored the subject in detail, but many questions remain unanswered.

[1] Richardson, L.F. 1925. *Big Whirls.*

The understanding of the transport of scalars in turbulent flows is also important to engineers. Turbulence serves to mix two fluids rapidly by increasing their contact area, thus allowing for faster molecular diffusion. Mixing of species, heat transfer and chemical reactions are all enhanced in turbulent flows. The prediction of these processes requires a thorough understanding of turbulent flows and the mixing of scalars therein.

1.1 Theory

Although turbulent flows are very common, they are difficult to predict. The Navier-Stokes equations, which describe fluid motion, are extremely sensitive to initial and boundary conditions when the flow is turbulent. A stochastic approach to turbulent flow is common as turbulence is random.

A passive scalar is a quantity that depends on the flow for its bulk transport and does not modify the nature of the flow. Its field is described by the advection-diffusion equation. The latter is a linear equation and one could hope that its solution might be deduced from the solution of the velocity field. However, "the accumulated knowledge over the past 30 years has shown this to be far from the case"[2]. In fact, since the advection-diffusion equation is simpler than the Navier-Stokes equations, and since turbulence mixes momentum and scalar in a similar manner, studies of scalar turbulence may offer insight into hydrodynamic turbulence.

[2] Warhaft, Z. 2000. Passive scalars in turbulent flows. *Annu. Rev. Fluid Mech.* **32**: p.205.

1.1.1 Turbulent flow

Understanding the governing equations of fluid motion is critical to any research in fluid mechanics. Assuming a constant property fluid, the Navier-Stokes equations (which express the principle of conservation of momentum) can be written (along with the expression for conservation of mass) in tensor notation as follows:

$$\frac{\partial u_i^*}{\partial x_i} = 0 \; ; \qquad \frac{\partial u_i^*}{\partial t} + u_j^* \frac{\partial u_i^*}{\partial x_j} = -\frac{1}{\rho}\frac{\partial p^*}{\partial x_i} + \nu \frac{\partial^2 u_i^*}{\partial x_j \partial x_j} . \tag{1-1}$$

At high Reynolds numbers, the Navier-Stokes equations become very sensitive to perturbations and the flow becomes chaotic. Consequently, the Navier-Stokes equations are intractable in this form for most applications pertaining to turbulent flow.

A common approach taken to rectify this problem is to separate instantaneous quantities (denoted by *) into the sum of their mean (capital letters) and fluctuations about the mean (lower-case letters). In other words, u* = U + u, which is called the Reynolds decomposition. Applying this decomposition and averaging the result (where averaged quantities are denoted by ‹ ›), the equation for the mean flow is:

$$\frac{\partial U_i}{\partial t} + U_j \frac{\partial U_i}{\partial x_j} + \frac{\partial \langle u_i u_j \rangle}{\partial x_j} = -\frac{1}{\rho}\frac{\partial P}{\partial x_i} + \nu \frac{\partial^2 U_i}{\partial x_j \partial x_j} . \tag{1-2}$$

An important term arises in equation (1-2). It is the average of the product of fluctuating quantities and is called the Reynolds stress. Its gradient is the mathematical difference between the instantaneous/laminar mean equations and turbulent ones.

The evolution of the fluctuations is expressed using their variance, ‹ $u_i u_i$ ›. It is called the turbulent kinetic energy budget and is derived using the instantaneous Navier-Stokes equations and the turbulent mean flow equation.

The Turbulent Kinetic Energy (TKE) budget, in tensor notation, is:

$$\frac{\partial}{\partial t}\left(\frac{1}{2}\langle u_i u_i\rangle\right)+U_j\frac{\partial}{\partial x_j}(\frac{1}{2}\langle u_i u_i\rangle)= \\ -\frac{\partial}{\partial x_j}\left(\frac{1}{\rho}\langle u_j p\rangle+\frac{1}{2}\langle u_i u_i u_j\rangle-2\nu\langle u_i s_{ij}\rangle\right)-\langle u_i u_j\rangle S_{ij}-2\nu\langle s_{ij}s_{ij}\rangle \quad (1\text{-}3)$$

The most important terms in equation (1-3) are:

$-\langle u_i u_j\rangle S_{ij}$	Production of TKE; exchange of energy with mean flow
$2\nu\langle s_{ij}s_{ij}\rangle$	Dissipation of TKE by viscosity

where $S_{ij}=\frac{1}{2}\left(\frac{\partial U_i}{\partial x_j}+\frac{\partial U_j}{\partial x_i}\right)$ is the mean fluctuating rate of strain and $s_{ij}=\frac{1}{2}\left(\frac{\partial u_i}{\partial x_j}+\frac{\partial u_j}{\partial x_i}\right)$ is the fluctuating rate of strain.

Turbulence occurs over a wide range of scales and varies in time and space. Large motions, on the order of the characteristic scale of the flow, transmit energy down to the smallest scales, where most of the energy dissipation occurs. This process is called the turbulent cascade. The large scales are called integral scales and the smallest ones are the Kolmogorov scales.

1.1.1.1 A categorization of turbulent flows

Turbulent flows can be categorized according to their level of complexity. In engineering problems, most flows are highly complex. Simplifying the flow in experiments helps to focus on fundamental aspects, e.g., the dissipation of turbulence.

The simplest turbulent flow is both homogeneous and isotropic (i.e., independent of coordinate translations, rotations and reflections). Grid turbulence is the most common

flow of this kind. A grid, of specified mesh size, placed in a wind tunnel produces quasi-isotropic turbulence. It is a laboratory flow and is rarely encountered in engineering situations. In grid turbulence, the TKE budget reduces to:

$$\frac{\partial}{\partial t}\left(\frac{1}{2}\langle u_i u_i \rangle\right) = -2\nu\langle s_{ij} s_{ij} \rangle . \tag{1-4}$$

The time rate of change of the TKE is balanced by its dissipation. In such flow, the decay of turbulent kinetic energy follows a power law, as shown by Comte-Bellot & Corrsin (1966).

Homogenous turbulent shear flows are more complex. A major study of the subject was performed by Tavoularis & Corrsin (1981). Using an array of parallel plates of prescribed length and roughness, a mean velocity gradient was created. At the exit of each passage, turbulence was generated by tripping the flow with a rod. Such experiments can be used to isolate the effects of shear, and therefore production, in turbulent flows.

At the third level of complexity are fundamental inhomogeneous turbulent flows. Common inhomogeneous turbulent shear flows include wakes, jets, mixing layers, boundary layers and fully-developped channel/pipe flows. The latter are inhomogeneous in the transverse direction only, whereas the first four are inhomogeneous in the downstream and transverse directions. In boundary layer and channel flows, the turbulence is non-decaying because of its constant generation by shear at the wall. The physics of these flows is discussed in Tennekes & Lumley (1972).

Finally, as explained before, the most difficult turbulence problems include the majority of practical applications and natural flows. In these cases, the turbulence can be strongly inhomogeneous in three directions and may or may not be decaying. By first understanding turbulent flows of lower complexity and then building on that knowledge, one can hope to someday fully comprehend the most complex of turbulent flows.

1.1.1.2 Wall-bounded turbulent flows

The present thesis involves wall-bounded turbulence. This term encompasses boundary layer and channel flows. The latter flow, studied herein, is of a high-aspect-ratio, is fully-developed and is statistically stationary. Following Tennekes & Lumley (1972), the mean momentum equations in such a flow reduce to:

$$0 = -\frac{1}{\rho}\frac{\partial P}{\partial x} - \frac{\partial \langle uv \rangle}{\partial y} + \nu \frac{\partial^2 U}{\partial y \partial y} \quad \& \quad 0 = -\frac{1}{\rho}\frac{\partial P}{\partial y} - \frac{\partial \langle v^2 \rangle}{\partial y}. \qquad \text{(1-5) \& (1-6)}$$

When non-dimensionalized, equation (1-5) becomes dependent on the Reynolds number, $\mathrm{Re} = \frac{Uh}{\nu}$, where h is the half-width of the channel.

By comparison, boundary layers are bounded by only one wall and their turbulence is inhomogeneous in both the transverse and downstream directions. The Navier-Stokes equations are thus more complex for boundary layers.

It is postulated that wall bounded flows can be separated in 4 zones: the viscous sublayer, the buffer layer, the log-law region and the outer layer. The relevant variables are a friction velocity (u*), a non-dimensional wall-normal distance (y^+) and a normalized mean velocity (u^+):

$$u^* \equiv \sqrt{\frac{\tau_w}{\rho}} \; ; \; y^+ \equiv \frac{u^* y}{\nu} \; ; \; u^+ \equiv \frac{U}{u^*}. \qquad \text{(1-7), (1-8) \& (1-9)}$$

In the viscous sublayer, $u^+ = y^+$. In the log law region, $u^+ = \frac{1}{k}\ln(y^+) + A$, where k (the von Karman constant) and A are constants with little dependence on the Reynolds number (Shah et al., 1983). The buffer layer connects the two zones. These results have been experimentally verified many times and will be compared to the mean velocity

profile in the channel used in this thesis (section 3.1.1). Pope (2000) defines the different regions as follows:

Region	Location
Viscous sublayer	y+ < 5
Buffer layer	5 < y+ < 30
Low-law region	30 < y+ and y/h < 0.3
Outer layer	y+ > 50

Table 1.1 Wall regions. h is the channel half-width.

It must be noted that the three first regions are equivalent for channel flows and boundary layers. However, the behavior of the outer layer differs because channel flow is bounded by two parallel walls whereas boundary layers are only bounded by one wall.

1.1.2 Scalar turbulence

Scalar transport is affected by the presence of the velocity in the advection-diffusion equation. Should the velocity field be turbulent, so will be the scalar field. The advection-diffusion equation is the basis for the study of scalar transport in a moving fluid, whether turbulent or not. In tensor form, it is:

$$\frac{\partial \theta^*}{\partial t} + u_j^* \frac{\partial \theta^*}{\partial x_j} = \gamma \frac{\partial^2 \theta^*}{\partial x_j \partial x_j}. \tag{1-10}$$

γ is the scalar's molecular diffusivity in the fluid under consideration. In the case of temperature, γ is the same as κ, the thermal diffusivity. Following steps analogous to the Reynolds decomposition of the velocity, the mean advection-diffusion equation becomes:

$$\frac{\partial \Theta}{\partial t} + U_j \frac{\partial \Theta}{\partial x_j} + \frac{\partial \langle \theta u_j \rangle}{\partial x_j} = \gamma \frac{\partial^2 \Theta}{\partial x_j \partial x_j}. \tag{1-11}$$

As before, capital letters denote mean values and lower-case letters, fluctuations. As with the Navier-Stokes equations, a turbulent (scalar) flux arises as the result of the decomposition.

The scalar variance equation, equivalent of the TKE budget, is:

$$\frac{\partial\langle\theta^2\rangle}{\partial t}+U_j\frac{\partial\langle\theta^2\rangle}{\partial x_j}+2\langle\theta u_j\rangle\frac{\partial\Theta}{\partial x_j}+\frac{\partial\langle u_j\theta^2\rangle}{\partial x_j}=-2\gamma\left\langle\frac{\partial\theta}{\partial x_j}\frac{\partial\theta}{\partial x_j}\right\rangle+\gamma\frac{\partial^2\langle\theta^2\rangle}{\partial x_j\partial x_j}. \quad (1\text{-}12)$$

A generalized form of equation (1-12) is more appropriate to the current work. It is the budget of scalar covariance, $\langle\theta_1\theta_2\rangle$, and is given by:

$$\begin{aligned}&\frac{\partial\langle\theta_1\theta_2\rangle}{\partial t}+U_j\frac{\partial\langle\theta_1\theta_2\rangle}{\partial x_j}+\langle\theta_2u_j\rangle\frac{\partial\Theta_1}{\partial x_j}+\langle\theta_1u_j\rangle\frac{\partial\Theta_2}{\partial x_j}+\frac{\partial\langle u_j\theta_1\theta_2\rangle}{\partial x_j}\\&=-2\gamma\left\langle\frac{\partial\theta_1}{\partial x_j}\frac{\partial\theta_2}{\partial x_j}\right\rangle+\gamma\frac{\partial^2\langle\theta_1\theta_2\rangle}{\partial x_j\partial x_j}\end{aligned} \quad (1\text{-}13)$$

The interpretation of the terms is as follows:

$\frac{\partial\langle\theta_1\theta_2\rangle}{\partial t}$	Time rate of change of covariance at a fixed point.
$U_j\frac{\partial\langle\theta_1\theta_2\rangle}{\partial x_j}$	Advection of covariance by the mean flow.
$\langle\theta_2u_j\rangle\frac{\partial\Theta_1}{\partial x_j};\langle\theta_1u_j\rangle\frac{\partial\Theta_2}{\partial x_j}$	Production of $\langle\theta_1\theta_2\rangle$ by mean scalar gradients.
$\frac{\partial\langle u_j\theta_1\theta_2\rangle}{\partial t}$	Turbulent advection of covariance by velocity fluctuations.
$\gamma\left\langle\frac{\partial\theta_1}{\partial x_j}\frac{\partial\theta_2}{\partial x_j}\right\rangle$	Molecular dissipation (or smearing) of covariance.

$\gamma \frac{\partial^2 \langle \theta_1 \theta_2 \rangle}{\partial x_i \partial x_i}$ Molecular transport (or diffusion) of covariance.

The relative complexity of turbulent channel flow makes it difficult to experimentally study the covariance on a term-by-term basis. Approaching the problem through the correlation coefficient and the coherency spectrum permits the quantification of the interaction of the scalars. They are non-dimensional forms of the covariance and the co-spectrum, respectively. The former is defined as:

$$\rho \equiv \frac{\langle \theta_1 \theta_2 \rangle}{\langle \theta_1^2 \rangle^{1/2} \langle \theta_2^2 \rangle^{1/2}}. \tag{1-14}$$

The scalar covariance arises in the expression of the total variance, defined as:

$$\langle (\theta_1 + \theta_2)^2 \rangle = \langle \theta_{1+2}{}^2 \rangle = \langle \theta_{12}{}^2 \rangle = \langle \theta_1^2 \rangle + \langle \theta_2^2 \rangle + 2\langle \theta_1 \theta_2 \rangle. \tag{1-15}$$

If the correlation coefficient is equal to ± 1, then the scalars are said to be either perfectly correlated (i.e. perfectly mixed) or perfectly anti-correlated. The correlation coefficient cannot be larger than unity from the Cauchy-Schwarz inequality.

The spectrum and co-spectrum are required for the computation of the coherency spectrum. They are defined as follows:

$$\Phi(f) \equiv \frac{1}{2\pi} \int_{-\infty}^{\infty} \left[e^{-ift} \right]_{REAL} \langle \theta^2 \rangle dt, \tag{1-16}$$

$$C_{\theta_1 \theta_2}(f) \equiv \frac{1}{2\pi} \int_{-\infty}^{\infty} \left[e^{-ift} \right]_{REAL} \langle \theta_1 \theta_2 \rangle dt. \tag{1-17}$$

Φ(f) is the power spectral density or spectrum. $C_{\theta 1 \theta 2}$(f) is the co-spectrum.

The coherency spectrum is a spectral analogue to the correlation coefficient. It is defined as:

$$\rho(f) \equiv \frac{C_{\theta_1\theta_2}(f)}{\left(\Phi_{\theta_1}(f)\right)^{1/2}\left(\Phi_{\theta_2}(f)\right)^{1/2}}. \tag{1-18}$$

The computation of the correlation coefficient and the coherency spectrum use the inference method, which is discussed in section 2.2.5.

1.2 Literature review

The total body of work on the subject of scalar turbulence is impressive and a literature review can therefore only be partial. The principal works of relevance to this thesis are summarized below.

Many books and reviews exist on turbulence and scalar turbulence. Important work includes books by Batchelor (1953), Hinze (1959), Monin & Yaglom (1971), Tennekes & Lumley (1972), Townsend (1976), Lesieur (1997), Baldyga & Bourne (1999) and Pope (2000). These books cover all aspects of turbulence. Reviews on scalar turbulence have been published by Sreenivasan (1991), Shraiman & Siggia (2000) and Warhaft (2000).

1.2.1 Turbulence measurements

Many turbulence measurement techniques exist, including: Hot-Wire Anemometry (HWA), Laser Doppler Anemometry (LDA) and Particle Image Velocimetry (PIV). The latter two were reviewed by Adrian (1996). In addition for scalar turbulence, Laser Induced Fluorescence (LIF) is commonly used (Walker, 1987). HWA is used for the present work. It is extensively reviewed by Comte-Bellot (1976), Perry

(1982) and Bruun (1995). It is a mature technique; the first writings on the subject date back to early 20th century (Comte-Bellot, 1976).

Depending on whether the sensor resistance or the current is kept constant, a hot-wire anemometer is considered either a Constant-Temperature Anemometer (CTA), also know as constant-resistance anemometer, or a Constant-Current Anemometer (CCA). The CTA has a very fast temporal resolution and is the most commonly used anemometer. Its sensor's temperature is set to be higher than that of the flow, and the latter's velocity is deduced from the resulting convective heat transfer. CCA systems do not have as good a frequency response as CTAs and are nowadays rarely used for velocity measurements. However, CCA systems can be modified and used as thermometers if the current is kept very low. In this case, the CCA sensor's temperature is directly proportional to the instantaneous local flow temperature. Paranthoën & Lecordier (1996) reviewed the measurement techniques for temperature in turbulence. Their work includes a large section on CCAs, which are used in the present thesis to make high-frequency temperature measurements.

1.2.2 Simulation techniques

Along with the development of computational power, the importance of simulations of turbulence has increased. Three principal approaches are commonly used in turbulence simulations: the Reynolds-Averaged Navier-Stokes method (RANS), Large Eddy Simulations (LES) and Direct Numerical Simulations (DNS). Pope (2000) discusses each of them.

In RANS, the turbulent fluxes are modelled so that the turbulent mean flow equations can be solved. RANS is the most common approach to turbulence simulations and it is the least computationally intensive. On other hand, DNS requires tremendous computational power and only relatively simple flows can be presently studied. DNS directly solves the Navier-Stokes and advection-diffusion equations and therefore directly

simulates the entire turbulent cascade. The possibilities offered by DNS are very promising but its challenges are daunting. LES, in short, solves the full equations up to a certain wavenumber and, from this point on, uses a model to approximate the smaller scales. It is less computationally demanding than DNS. Jaberi & Colucci (2003) detail LES approaches to scalar turbulence.

1.2.3 Scalar dispersion from single sources

The dispersion of a scalar from one source in turbulent flows has been extensively discussed in the literature. In most cases, temperature was the injected scalar. Dispersion in grid turbulence was the first to be studied. In this case, temperature can be injected into the flow by means of line sources or by heating the grid. Scalar dispersion experiments in grid turbulence were made by Taylor (1935), Uberoi & Corrsin (1953), and Townsend (1954). They published results on the evolution of the mean and fluctuating temperature fields.

The thermal wake from a line source in homogeneous, isotropic turbulence can be divided in three stages: 1) the molecular diffusive range, for which $t << \frac{\kappa}{\langle v^2 \rangle}$, where t is time, κ is the thermal diffusivity and v the transverse velocity fluctuation, 2) the turbulent convective range, $\frac{\kappa}{\langle v^2 \rangle} << t << t_L$, where t_L is the Lagrangian timescale, and 3) the turbulent diffusive range where $t >> t_L$. The study of thermal fields emitted from line sources in grid turbulence was thoroughly studied by Warhaft (1984). For a single line source, he presents results for mean, RMS and spectral quantities.

In grid turbulence, the mean temperature profiles are Gaussian for a certain range of downstream distances from the source. The half-width of the Gaussian profile (defined as half the width of the profile when its level is 50 % of its maximum value) increases as $t^{1/2}$ in the first range, then linearly in the turbulent convective range and finally, in the last

stage, is proportional to $t^{1/2(2-n)}$, where n is the decay exponent of $\langle v^2 \rangle$ and takes on values close to 1 (Warhaft, 1984; Stapountzis et al.,1986). The temperature RMS (θ_{rms}) profile is initially double-peaked, a phenomenon which disappears and then reappears when the thermal plume is much larger than the integral scale.

Karnik & Tavoularis (1989) measured the diffusion of heat from a line source in a homogeneous, uniformly-sheared, turbulent flow. The source was placed perdendicular to the flow and parallel to the shear-generating plates. They found that the mean scalar profile slowly drifted from behind the source location towards the lower velocity region. The appearance, disappearance and re-appearance of double peaks in the transverse profiles of θ_{rms} were also observed. The initial double peak can be traced back to the bulk flapping of the thermal wake. The second appearance was explained by Karnik & Tavoularis (1989) as follows. Far downstream, when the plume is wide, large eddies have only secondary effects on the temperature fluctuations. The production term in the variance equation (equation 1-12) is a function of the mean temperature gradient. At the mean profile peak, the mean temperature gradient is zero. Therefore the production of variance is reduced in the central region of the thermal wake and the local θ_{rms} value decreases. The situation in turbulent channel flow is different. As Lavertu (2002) noted: "it is [...] expected that double peaks (far downstream) in the RMS profiles will not occur in bounded flows"[3] as the plume width is limited by the walls and will therefore never be much larger than the largest eddies.

Inhomogeneous shear flows are usually divided into two families: wall-bounded shear flows and free-shear flows. The first includes boundary layer flows and internal flows. The latter includes wakes, jets and mixing layers.

Lavertu & Mydlarski (2005) studied the scalar mixing from a single line source in fully-developed turbulent channel flow. They used three line source positions and took measurements at 6 downstream locations. The source was positioned in a similar manner to the ones used in the present work (parallel to the wall and perdendicular to the flow).

[3] Lavertu, R. 2002. *Scalar dispersion in turbulent channel flow.* M. Eng. Thesis, McGill University, p.15

Their results include mean profiles, RMS profiles, PDFs, skewnesses and velocity-temperature correlations. The mean and RMS profiles were well approximated by truncated Gaussian distributions. Important differences were shown between turbulent channel flow, grid-generated turbulence (Warhaft, 1984) and homogeneous shear flow (Karnik & Tavoularis, 1989) (such as the displacement of the peak RMS temperature towards the centreline in channel flow).

Fundamental work on scalar dispersion in boundary layers was done by Poreh & Cermak (1964) and Poreh & Hsu (1971). They studied the diffusion from a line source in neutrally buoyant conditions. They divided the evolution into four stages[4]:

1. Initial stage close to the source.
2. Intermediate stage, [...] in which the concentration profiles are found to be approximately [self] similar.
3. Transition stage with [a] somewhat slower growth of the diffusion layer.
4. Final stage in which the diffusion is limited by the growth of the developing boundary layer.

Shlien & Corrsin (1976) studied the mean temperature profiles of a line source placed at different elevations in planar boundary layers. They found that the "mean temperature profiles approached nearly the same asymptotic shape in all cases"[5]. The dispersion from a line source in both a plane jet and a boundary layer was examined by Paranthoën et al. (1988). They developed and applied a rescaling scheme based on the Lagrangian integral time-scale of the wall-normal velocity fluctuations at the source location. Their work was successful in collapsing the mean peak temperature onto a simple curve. Additional research on the subject was performed by El Kabiri et al. (1998), who tested various second-order and third-order closure models on experimental data measured in a boundary layer. Increasing the complexity of the flow, Vinçont et al.

---

[4] Poreh, M. & Hsu, K.S. 1971. Diffusion from a line source in a turbulent boundary layer. *Int. J. Heat Mass Transfer* **14**. p.1475

[5] Shlien, D.J. & Corrsin, S. 1976. Dispersion measurement in a turbulent boundary layer. *Int. J. Heat Mass Transfer* **19**, p.285

(2000) studied the dispersion from a line source placed in a boundary layer, downstream of an obstacle.

Scalar turbulence in the turbulent wake of a circular cylinder was studied by Beaulac & Mydlarski (2003). They injected the scalar using an array of thin wires (called a "mandoline") behind the cylinder and studied the effect of changes in the thermal field initial conditions on its downstream evolution. Scalar turbulence in mixing layers was the subject of a study by Veeravalli & Warhaft (1990). It was studied in jets by Incropera et al. (1986), Grandmaison et al. (1991) and Tong & Warhaft (1995).

Hanratty and coworkers have made multiple numerical studies of scalar mixing in inhomogeneous flow. His group studied scalar dispersion in low-Reynolds-number channel flow (Lyons & Hanratty, 1991; Papavassiliou & Hanratty, 1997; Na & Hanratty, 2000). Kontomaris & Hanratty (1994) studied the effects of molecular diffusivity on a point source located at the centreline of a turbulent channel flow and Iliopoulos & Hanratty (1999) simulated the dispersion of fluid particles in inhomogeneous turbulence.

Other computational works include that of Bernard & Rovelstad (1994), who examined the accuracy of a scalar transport model in inhomogeneous turbulence. The turbulent mixing of a passive scalar in pipe flow emitted from a point source was investigated by Brethouwer et al. (1999). Orlandi & Leonardi (2004) simulated the behaviour of a passive scalar in turbulent channel flow with wall velocity disturbances in an attempt to emulate rough-wall channels.

1.2.4 Scalar dispersion from multiple sources

Warhaft (1984) extended his work on scalar mixing in grid turbulence by studying the interference of two thermal line sources. He determined the correlation coefficient between both scalars (ρ) at 8 downstream positions for 10 different separation distances between the line sources (d). His results show that the evolution of ρ is a function of two

parameters: the non-dimensional separation distance $\left(\frac{d}{\ell}\right)$, where ℓ is the integral length scale, and the non-dimensional downstream distance $\left(\frac{x'}{d}\frac{u}{U}\right)$, where x' is the distance from the line sources, u the longitudinal RMS velocity and U the mean (longitudinal) velocity. He completed his work by experimenting with multiple line sources in an attempt to reinterpret the scalar variance produced by a mandoline.

Tong & Warhaft (1995) investigated the mixing characteristics of temperature fluctuations produced by two fine annular sources placed axisymmetrically at a given downstream position in a turbulent jet. They found that the scalar covariance was strongly dependent on the ring locations and that, in 1.5 eddy turnover times, the mixing was complete in all situations. Their coherency spectra increased faster at large scales than at small scales and they found faster rates of mixing in a jet than in grid turbulence (Warhaft, 1984).

To aid in modeling competitive-consecutive reactions (reactions where the first is of the form A + B → C and a subsequent one is of the form A + C → D), Vrieling & Nieuwstadt (2003) numerically studied the turbulent dispersion from nearby point sources in channel flow. They calculated the scalar covariance resulting from line sources located symmetrically around the channel centreline. They assumed that, in the central region of the channel, the flow was almost homogeneous. Their results were in agreement with those published by Warhaft (1984) for grid turbulence.

1.3 Objectives

The objective of the present thesis is the quantification of the interaction between two scalars generated by line sources in fully-developed, high-aspect ratio, turbulent channel flow. Studying the scalar mixing process in inhomogeneous turbulence will serve to further our understanding of similar phenomena in more realistic flows, such as the

atmosphere, internal combustion engines and chemical reactors. Furthermore, in studying inhomogeneous flows, the present work will expand upon previous experiments. To the author's knowledge, the computation of the correlation coefficient and of the coherency spectra of two scalars in a bounded flow has not been previously measured. Thus, the present work should add to the body of knowledge in this area.

1.4 Thesis overview

Following this introduction to the current work, the experimental apparatus and measurement techniques will be presented in Chapter 2. The latter contains detailed information on the experimental facility, the coordinate system, the measurement techniques, their calibration and their resolutions. Finally, the acquisition of data is discussed.

In Chapter 3, the experimental conditions and the flow properties are evaluated. The present work is based on the following assumptions: fully-developed channel flow, a passive scalar, adiabatic walls and a 2D scalar field. All these characteristics will be analyzed and verified. An error analysis and a list of flow properties will also be included in Chapter 3.

Results will be presented in Chapter 4 for the mixing of two scalars with multiple combinations of source locations. The following quantities will be discussed:

1. Scalar field statistical moments
2. Scalar correlation coefficients
3. Scalar co-spectra and coherency spectra

Comparisons will be made with previous relevant experiments and simulations. A bibliography of the cited authors completes this thesis.

2. Experimental apparatus

The turbulent channel flow wind tunnel of McGill University's Aerodynamics Laboratory was used in this study. The temperature measurements were made with a cold-wire thermometry system. All information pertaining to these elements is discussed in this chapter.

2.1 Experimental facility

The wind tunnel design was the subject of an honours thesis by McLeod (2000). The latter contains detailed information on the channel specifications and characteristics. The facility was subsequently used by Lavertu (2002) for his master's thesis.

Some changes were made to the channel for this study. Firstly, the alignment of the channel walls was improved. To accomplish this, extra pressure points were installed on the external face of one of the channel walls. Further proof of the symmetry of the flow will be provided in section 3.1. Secondly, the line source insertion method was also improved. The new method no longer requires the removal of a channel wall to move the line sources. It also permits more freedom in the selection of the source locations.

2.1.1 Detailed description

The facility is an open-circuit channel wind tunnel. It can be divided into three sections: the blower, the flow conditioner and the constant-cross-section channel test section. The air flow is provided by a Hudson Buffalo centrifugal blower. It is powered by a 7.5 hp (5.6 kW) AC motor. The motor is controlled by an ABB ACS 600 frequency converter. It allows precise control of the motor RPM and hence the air flow rate. The blower and its motor are mounted on vibration pads. A series of filters are placed at the blower intake, preventing particles larger than 0.3 μm from entering the channel and potentially damaging the instrumentation.

To further insulate the channel from the motor vibrations, a flexible coupling joins the blower outlet to the inlet of the channel's flow-conditioning section. The purpose of the flow-conditioner is to transform the irregular flow coming from the 0.45m x 0.33 m exit of the blower into a regular, organized flow suitable for experimentation. As a preliminary means for reducing the flow irregularities, the air first passes through a perforated plate at the blower exit. The velocity of the air in the flow-conditioner is reduced by using a diffuser. To diminish its length, its angle is 45 degrees. With such a large diffuser angle, the flow would normally separate. However, the resulting adverse pressure gradient is offset by four screens appropriately positioned inside the diffuser. They balance the pressure rise (arising from the decreasing velocity) by a corresponding pressure drop (resulting from the screens) (Mehta, 1977).

The settling chamber continues to reduce the undesired effects from the blower. Its cross-section is constant and matches that of the diffuser exit. In the settling chamber, the flow first encounters an aluminium honeycomb section. A set of six screens follows the honeycomb. McLeod (2000) provides detailed information on their sizes and locations.

The contraction links the settling chamber to the channel test section. A fifth-order polynomial was used to design the contraction, as recommended by Reshotko et al. (1997). The flow entering the channel is uniform and has a low turbulence intensity (0.25%).

Shortly after entering the test section, two tripping rods are positioned 3mm away from the walls. Their purpose is to accelerate the formation of a fully-developed flow, by prematurely inducing the boundary layers to become turbulent. At the exit of the channel, a honeycomb similar to the one in the settling chamber is placed to dampen any external flow disturbances and preserve the fully-developed flow characteristics inside the test section.

The channel test section is 8 m long, 1.1 m high and 0.06 m wide. Its aspect ratio (18.3) is large enough to ensure that the bottom and top wall do not affect the flow field in the center of the channel, where all measurements are made. The walls are made of nominally 0.0254 m thick Plexiglas sheets joined by means of "biscuits". The channel walls can be considered hydraulically smooth because their maximum roughness is less than 5 viscous lengths (Tennekes & Lumley, 1972), which corresponds to 0.15mm for the mean flow used herein. The top and bottom channel walls are T-shaped Plexiglas caps. As previously mentioned, adjustable tightening screws are used to adjust the channel width.

The experiments are performed towards the end of the channel where the flow is fully-developed (Lavertu, 2002). Two circular openings were made in one of the channel's walls to allow for the insertion of probes. In the caps, three openings were made to insert the line sources. When they are not required for testing, the openings are plugged so that the top and bottom walls are smooth. When an opening is needed for insertion of a line source, a special plug is used. A linear traversing mechanism, controlled by a precision stepper motor (0.01mm per step), is used to move probes across the channel.

2.1.2 Coordinate system

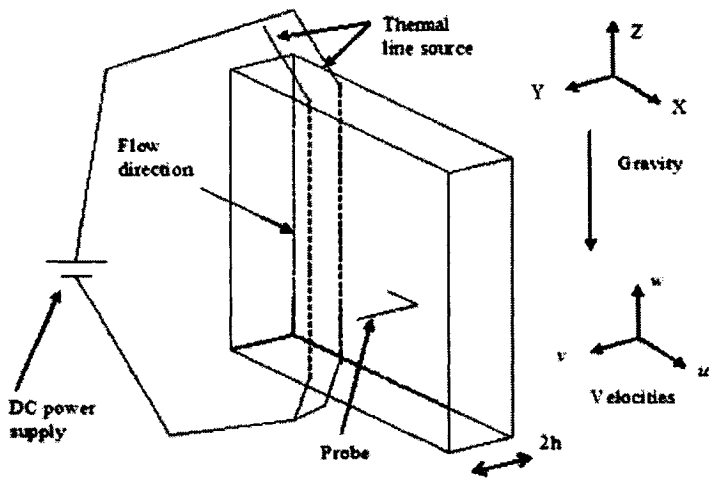

Figure 2.1 Coordinate system

Figure 2.1 presents a schematic of the experimental setup and the coordinate system used in the channel. The Y-direction corresponds to the transverse direction. Its zero position is along the channel wall opposite to the one in which the probe is inserted. The X-direction is in the streamwise direction and is taken to be zero at the line source location. The fully-developed nature of the flow permits the movement of sources instead of the probe to vary the downstream distance. Therefore the X-coordinate is not an absolute measure of the position in the channel but rather a downstream distance from the source. The Z-axis is parallel to the height of the channel and the gravitational vector. Outside of the top and bottom regions, the flow field is independent of Z. All measurements are made at 0.55 m, far from any end effects (Lavertu, 2002).

2.1.3 Scalar injection

Fine line sources made of Nichrome^{TM} are placed vertically in the channel to inject the scalar (temperature). They are kept taut (using weights attached to their ends) to counteract their thermal expansion when heated. Both ends are connected to the terminals of a DC power supply. The line sources are inserted through openings in the caps. To secure their positions (X & Y), aluminium plugs with precisely positioned (0.6 mm diameter) holes are installed. Each hole is electrically insulated from the others by the insertion of glass micro-capillary tubes (0.3 mm internal diameter). The source diameter is small enough to be passed through the appropriate hole for each experiment.

The Kepco DC power supply heating the line sources has an output voltage accuracy of 0.01%. To assure that the power going through the line sources is constant, the voltage across them was continuously monitored.

The use of two different line source diameters was required to obtain satisfactory signal-to-noise ratio at large downstream distances. Line sources of 0.127mm diameter were used for measurements at x/h = 4.0 and 7.4. In these cases, the power passing through each line source was 45 W/m. For the other downstream distances, line sources

of 0.254 mm diameter were used. The corresponding power was 100 W/m. The difference between the inputted powers will be taken into account in Chapter 4. The measurements made using 100 W/m are divided by 2.22 for mean and RMS temperature measurements and by 2.22^2 for temperature spectra to be compared with measurements made using 45 W/m.

Distances are normalized by the half-width of the channel, h = 0.03 m. The positions of the line sources are specified in terms of their average position (y_{s_av}) and the distance between the two lines sources (d). For example, if the two line sources have a distance between them of d/h = 1.50 and an average position of $y_{s\_av}/h = 1.0$, then their corresponding positions with respect to the wall are y/h = 0.25 (y = 7.5mm) and y/h = 1.75 (y = 52.5mm).

In total, 54 different cases are studied. Six downstream distances are used: x/h = 4.0, 7.4, 10.8, 15.2, 18.6 and 22.0. Nine combinations of wall-normal source locations were chosen. These combinations cover the regions of interest in the channel. Table 2.1 presents the line source positions that are used. This information is graphically shown in Figure 2.2.

		Average Position ($y_{s\ av}/h$)		
		0.2	0.5	1.0
Distance (d/h)	0.13	X	X	X
	0.27	X	X	X
	0.50		X	X
	1.50			X

Table 2.1 Line sources combinations. Shaded combinations are not possible.

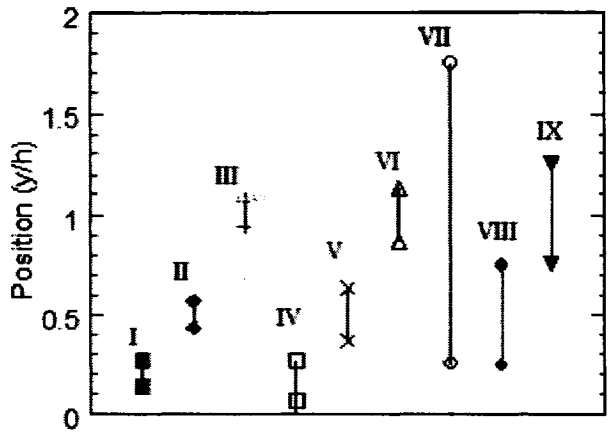

Figure 2.2 Visualization of the 9 pairs of line source locations

2.2 Measurement techniques

Three different measurement techniques were employed herein: Hot-Wire Anemometry (HWA), Cold-Wire Thermometry (CWT) and mean temperature excess measurements by use of thermistors.

2.2.1 Hot-wire anemometry

Velocity measurements are required to describe the flow field in which the scalar is being transported. A copper-coated tungsten wire (with a 3 μm diameter core) is mounted on a TSI 1240 probe or a TSI 1218 probe (specially made for near-wall measurements). The wire is then etched with acid to expose a portion of the core.

Using a TSI IFA 300 anemometer, the wire is heated to a temperature above that of the flow, which is maintained by electronic circuitry that keeps the wire resistance constant. The latter is set to 1.8 times the room temperature resistance. The change in the air speed is determined from the change in the voltage that must be supplied to keep the wire resistance constant. The HWA calibration curve (Figure 2.3) relates air speed and

anemometer voltage. The data are fit to King's Law: $E^2 = A + BU^N$, where A, B & N are constants. The constants are obtained through a least-squares curve fit.

The calibration is performed by placing the hot-wire sensor at the exit of the nozzle of a TSI 1127 calibration jet. The jet velocity is determined using a precision MKS 220D pressure transducer. A number of voltage readings are taken with the probe at different velocities. The calibration range covers the range of possible experimental velocities. The density of calibration points must be greater at beginning of the plot where the curvature is larger (Bruun, 1995). Amplification and offsetting of the signal are performed through the IFA300 control software when required.

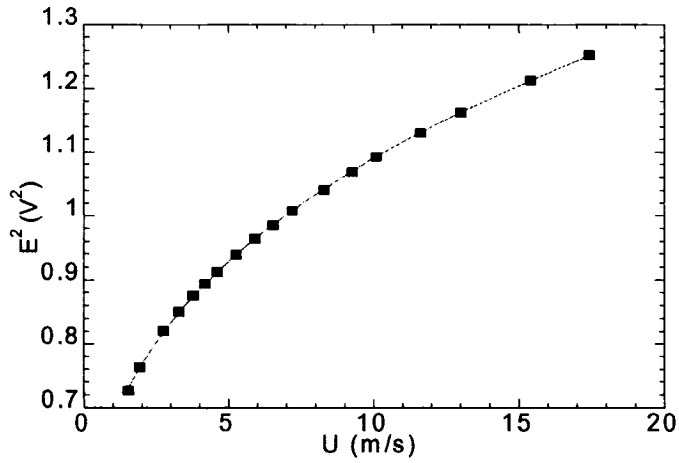

Figure 2.3 Hot-wire calibration curve

2.2.2 Cold-wire thermometry

The sensing part of a CWT system is a platinum-rhodium (90%-10%) Wollaston wire of diameter 0.63 μm. It is mounted on a TSI 1240 single-wire probe. The Wollaston wire is soldered on the probe and its central section is then etched to reveal its platinum-rhodium core.

The thin platinum-rhodium wire has a very low thermal inertia and can react to rapid changes in the local temperature. A constant-current anemometer circuit built at the

Université Laval in Québec is connected to the probe. It passes a very small, constant current through the wire. The wire resistance will change according to the local flow temperature. By measuring the voltage across the sensor, its resistance, which varies linearly with temperature, can be deduced by R = E/I. The voltage must be amplified since the temperature variations do not lead to great changes in resistance. The calibration relation is thus: T= AE + B, where A and B are constants.

It is important to keep the current low to maintain the wire temperature very close to the local flow temperature. If the wire is heated by the current, it can be cooled by convection and becomes sensitive to velocity fluctuations. The current used (0.1 mA) is a balance between such velocity-induced effects and maintaining a strong signal-to-noise ratio.

The calibration is performed using a TSI 1127 calibration jet. It produces a jet of heated air at constant velocity. The jet temperature is allowed to decrease and its instantaneous value is given by a reference thermocouple. Measurements are taken at different temperatures to calibrate a sensor (Figure 2.4). To minimize non-linear effects, the calibration is made as close as possible to the experimental temperature.

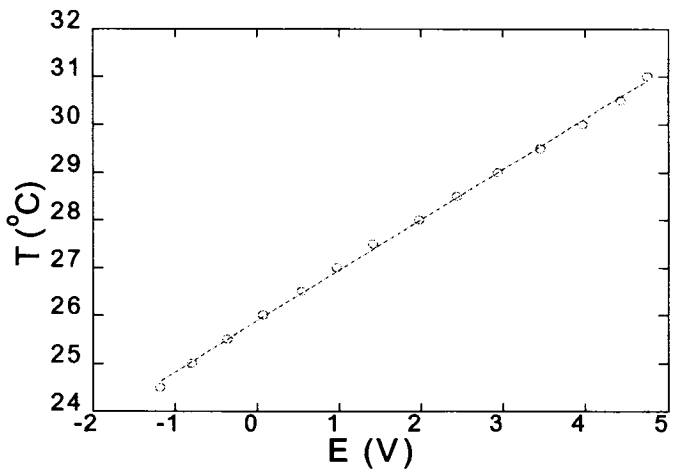

Figure 2.4 Cold-wire calibration curve

2.2.3 Mean temperature measurements

To measure the upstream temperature, a Sensor Scientific glass bead thermistor is placed 1.6m away from the probe. The thermistor resistance is very sensitive to temperature variations and changes by more than 300 Ω per degree in the temperature range of interest. Its temporal resolution is around 1 Hz. Mean excess temperature values are computed by subtracting the thermistor temperature reading from the mean CWT temperature reading.

2.2.4 Spatial and temporal resolution of the probes

It is desirable to be able to capture all the turbulent cascade's length-scales and time-scales with the instrumentation. To do so, it must have time constants that are smaller than the smallest time-scales of the flow. Similarly, the sensor size must be smaller than the smallest length-scales of the flow. These are called the Kolmogorov microscales:

$$\eta \equiv (\nu^3 / \varepsilon)^{1/4} \text{ [m]}, \tag{2-1}$$

$$\tau \equiv (\nu / \varepsilon)^{1/2} \text{ [s]}. \tag{2-2}$$

η is the Kolmogorov length-scale, τ is the Kolmogorov time-scale, ε is the dissipation rate of turbulent kinetic energy and ν is the kinematic viscosity. The values of the Kolmogorov microscales are presented in section 3.4. In the present work, the Oboukhov-Corrsin scales, the scalar equivalent of the Kolmogorov scales, are of interest. The thermal diffusivity (κ) is responsible for dissipation of temperature variance in the same way that viscosity (ν) dissipates kinetic energy. Their ratio, the Prandtl number (ν/κ), is of the order of one (precisely 0.71); therefore, the hydrodynamic and scalar micro-scales are almost equal.

According to Lemay (2001), a 0.63 μm cold-wire is able to resolve to frequencies of 7.3 kHz at 5 m/s. The frequencies of the microscales are between 2.5 kHz and 3.5 kHz. Thus, the CWT has a sufficient temporal resolution for this study. However, if the flow velocity were increased, it is probable that the temporal resolution could be too low. Lemay & Benaïssa (2001) propose compensation measures for such cases.

Cold-wire thermometers have lower frequency responses than CTAs. This is why CTA is preferred to CCA for velocity measurements in modern aerodynamics laboratories. The frequency response of the TSI IFA 300 system is flat up to 100 kHz. The temporal resolution of the velocity measurements is therefore a non-issue in the present experiments.

With respect to the spatial resolution, it will be shown in Table 3.4 that the Kolmogorov microscales are between 0.15 mm and 0.28 mm. The sensors' working lengths are usually around 0.5 mm for both the HWA and CWT probes. Wyngaard (1968 & 1971) presents correction curves for velocity and temperature spectra. From his results, the measured value of the temperature spectra will be 90 % of the exact value at 2 kHz. Most measurements will be made at a sampling frequency of 200 Hz. In that range, the measured values will be of 99 % of the exact values. The spatial resolution is thus sufficient at this frequency/wavenumber. When required, Wyngaard's compensation will be applied to the spectra.

2.2.5 Inference method

The inference method is used to determine the scalar correlation coefficients and the coherence spectra. It employs a sequence of measurements of θ_{12}, θ_1 and θ_2 to infer the previous quantities (Warhaft, 1984). This method is adequate if the flow conditions and the scalar injection rates remain constant.

By using equation (1-14) and (1-15), it is possible to rewrite the correlation coefficient as:

$$\rho = \frac{\langle \theta_{12}^2 \rangle - \langle \theta_1^2 \rangle - \langle \theta_2^2 \rangle}{2\langle \theta_1^2 \rangle^{1/2} \langle \theta_2^2 \rangle^{1/2}}. \tag{2-3}$$

All quantities in equation (2-3) can be measured in a straight-forward manner by CWT and thus the covariance (and therefore the correlation coefficient) can be inferred.

Using equation (1-15), the covariance can be replaced in the definition of the co-spectrum, which becomes:

$$C_{\theta_1\theta_2}(f) = \frac{1}{2}\left[\Phi_{\theta_{12}}(f) - \Phi_{\theta_1}(f) - \Phi_{\theta_2}(f)\right]. \tag{2-4}$$

The electrical circuits used to power the two line sources were designed to be identical. The line source resistances are adjusted to be equal when they are installed in the channel. To monitor the power level in the line sources, a voltmeter is connected to their ends. This ensures that the rate of scalar injection in the flow remains constant for the four-hour duration of one experiment.

The inference method does not require equal power passing through each line source, only constant power. Unequal power levels will not change the value of the correlation coefficient. However, the RMS and mean profiles would be affected. Equal power is therefore used for simplicity.

2.3 Acquisition setup

2.3.1 Acquisition system

The signals produced by the CWT and HWA need to have the unwanted noise filtered out. A Krohn-Hite model 3382 band-pass filter is used for all measurements. The signal is low-pass filtered to eliminate any high-frequency noise at frequencies above the Kolmogorov microscales. All measurements are also high-pass filtered to eliminate any low-frequency and non-turbulent fluctuations such as those that might result from a drift in mean ambient temperature, etc..

The analog signals from the CWT and HWA are digitized using a 16-bit National Instruments PCI-6036E board. It can sample at rate of to 200,000 samples per second. This is fast enough for the present work. Before sampling, the range over which the voltage will be digitized is selected. This range is divided by 2^{16} to give the conversion precision. In the range typically used (± 5 V), the manufacturer lists an absolute accuracy of 1.790 mV.

The data acquisition is performed using programs written in LabView 7.0. Subsequent statistical analysis of the acquired data is performed by a computer code written in FORTRAN 90.

2.3.2 Sampling

The nature of the sampling for this experiment can be divided into sampling for spectral data sets and sampling of Probability Density Function (PDF) data. The purpose of the former is to obtain information on the properties of the data over all frequencies in the flow. The latter is used to determine the statistical moments of the data.

The sampling made for spectral data sets is performed at twice the Kolmogorov time scale (approximately 7 kHz) in accordance with the Nyquist criterion. For these measurements, 100 blocks of 4096 data are taken. Thus a data set is made of 409,600 points. Power spectra are calculated by means of Fast Fourier Transforms (FFTs) of spectral data sets.

The PDF (theoretically) contains all information about the statistical moments. Each moment is defined by:

$$\langle \theta^n \rangle = \int_{-\infty}^{\infty} \theta^n P(\theta) d\theta . \tag{2-5}$$

$P(\theta)$ denotes the PDF at a given value of θ. To compute $\langle \theta^n \rangle$, equation (2-5) requires that the convergence has been reached for all moments. Note that convergence of $P(\theta)$ in the tails of the PDF can be very slow for high-order moments.

A surrogate method for the computation of statistical moment from a finite data set is:

$$\langle \theta^n \rangle = \lim_{T\to\infty} \frac{1}{T} \int_0^T \theta^n dt . \tag{2-6}$$

Convergence is relatively fast for low-order moments and equations 2-5 and 2-6 will, in such cases, provide the same result. The output signal for the mean converges in approximately 60 seconds (Table 2.2).

Seconds	Vdc
1	5.0271
10	5.0153
15	5.0239
20	5.0205
30	5.0186
60	5.0189

Table 2.2 Mean convergence

For the higher moments, the sampling rate must be wisely selected to develop an efficient acquisition process. Tennekes & Lumley (1972) suggest to sample at a frequency equal to the inverse of the integral time-scale. In the present case, it is around to 200 Hz, though it depends on the transverse location of the sensor. Here again, blocks of 4096 points are taken. Table 2.3 presents the convergence of the second, third and fourth statistical moments. From these results, it was decided to use 10 blocks of data. This represents 3 minutes 25 seconds of sampling for each position.

Number of blocks	υ_{RMS}	S(υ)	K(υ)
1	0.25508	1.045	3.7662
5	0.24885	1.0365	3.9217
10	0.25013	1.0122	3.8297
20	0.25018	1.0228	3.8353
50	0.25021	1.0168	3.8372

Table 2.3 Moment convergence

The last point concerns the PDF convergence. The sampling is done at 200 Hz for the previously cited reasons. Figure 2.5 shows that 50 blocks (17 minutes) gives an excellent quality of results compared with 100 blocks (34 minutes).

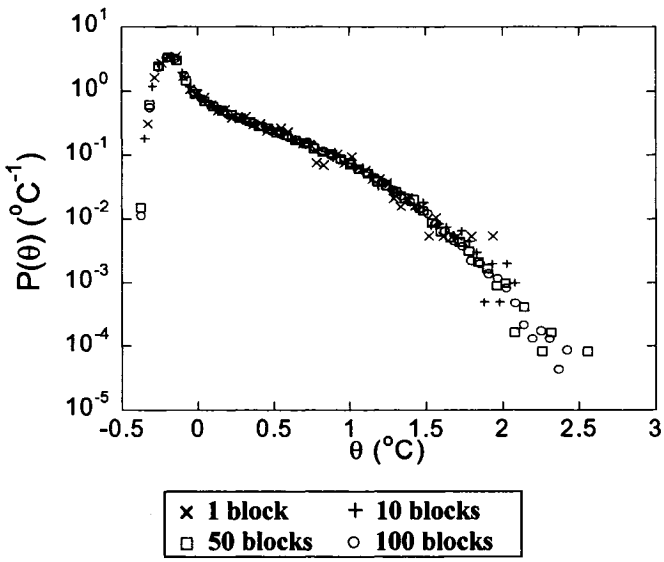

Figure 2.5 PDF convergence

3. Experimental conditions, sources of error and flow properties

3.1 Verification of the experimental conditions

The present work is based on the following assumptions, which relate to the nature of the flow:

1. The velocity field is fully-developed.
2. The scalar fluctuations are passive.
3. The channel walls are adiabatic.
4. The scalar field is independent of the Z-direction.

Each of the above assumptions was discussed in detail by Lavertu (2002) and is summarized below.

3.1.1 Fully-developed, one-dimensional channel flow

For the present work, the velocity profile is constant in the downstream direction and only varies in the wall-normal direction. This property was verified by McLeod (2000) and Lavertu (2002) in the apparatus used herein. As modifications were made to the channel which could have affected the flow field, the fully-developed nature of the flow was again verified.

For velocity measurements done at ports 8-1 and 8-2, the maximum difference in the mean, RMS, skewness and kurtosis profiles are respectively: 1.1 %, 3.8 %, 6.1 % and 2.2 %. The relatively large difference in the skewness results from the fact that its value is close to zero. It is worth noting that the absolute errors are small. The constancy of the

high-order moments is a better indicator of a fully-developed turbulent flow (Shah et al., 1983) than measuring the pressure gradient or the mean velocity profile.

Figure 3.1 compares the mean flow profile with the log-law (section 1.1.1). The friction velocity for channel flow is determined using the pressure drop, (Tennekes & Lumley, 1972):

$$u^* = \sqrt{\left|\frac{dP}{dx}\right| \frac{h}{\rho}}. \tag{3-1}$$

The pressure drop was 2.6 Pa/m which corresponds to a friction velocity of 0.256 m/s. The four zones discussed in section 1.1.1 are well defined although the first one does not respect $u^+ = y^+$ due to the lack of data and the imprecision in measuring near-wall positions.

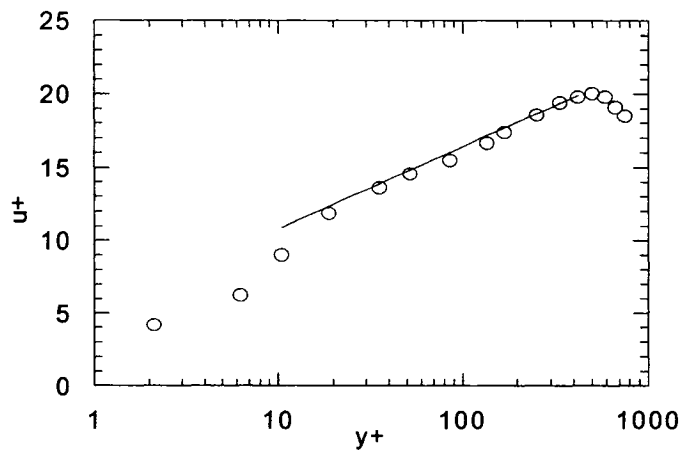

Figure 3.1 Mean velocity profile, in terms of u+ & y+. The line represents the (theoretical) log law.

The independence in the Z-direction of the velocity profile was proven by McLeod (2000). Based on his results, it is assumed that the flow and thermal fields are independent of Z in the middle portion of the channel.

3.1.2 Passive scalar fluctuations

By definition, a passive scalar does not affect the flow field. The scalar can produce two possible disturbances:

1. Buoyancy effects.
2. Creation of flow disturbances by the presence of the line sources.

Body-force-generated scalar turbulence is complex. It adds a turbulence production term $\left(\frac{g_i}{T}\langle\theta u_i\rangle\right)$ in equation (1-3). To evaluate its importance, it is customary to compare it to the dissipation of TKE (ε). The temperature-velocity correlations in the present flow were thoroughly measured by Lavertu (2002). His conservative estimate of the ratio of buoyant production to dissipation is at most 1.7%. Thus the scalar can be considered to be passive.

The critical Reynolds number for vortex-shedding behind a cylinder is 40 (Blevins, 1990). For Reynolds numbers below this value, the generated wake is almost instantaneously damped out. Following the calculations presented by Lavertu (2002), the Reynolds number for the large line source (0.254 mm diameter) is found to be 44. For the small line source (0.127 mm diameter), the Reynolds number is 27. Consequently, it is not expected that vortex-shedding will significantly affect the flow (Lavertu, 2002).

3.1.3 Adiabatic channel walls

To minimize external disturbances, the channel should be insensitive to the outside conditions. The loss of injected heat through the walls could lead to important errors. Lavertu & Mydlarski (2005) have shown that the mean-excess temperature is effectively zero near the wall when the line is centered at y/h = 1. This suggests that there is no heat transfer through the wall when the line source is far from it. When the line

source is closer to the wall, the maximum heat loss is around 1.5% and therefore the channel walls can be considered to be virtually adiabatic (Lavertu, 2002).

3.1.4 Two-dimensional scalar field

In a fully-developed flow, the scalar source can be displaced in the X-direction and the resulting scalar field will be translated but not changed. This allows a moving reference in the downstream direction, as explained in section 2.1.2. Lavertu (2002) verified that this was the case and the current work shares the same experimental conditions. Lavertu (2002) also showed that the thermal fields produced by 0.127mm and 0.254 mm diameter line sources were statistically identical and therefore independent of the line source diameter.

Figure 3.2 confirms the symmetry of the channel walls and of the thermal field about the channel's centreline.

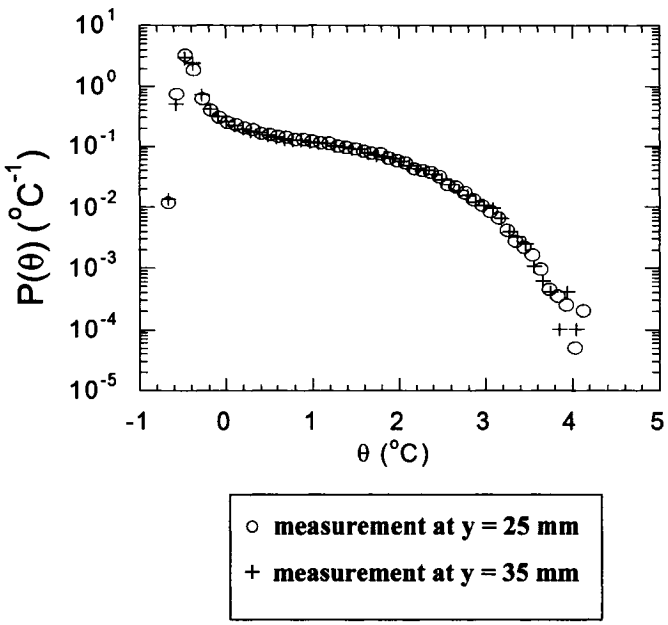

Figure 3.2 Symmetry test of P(θ) at x/h = 4.0 for line source located at y/h = 1.0 (y = 30 mm).

An additional confirmation of the scalar field symmetry is provided in Figure 3.3. The RMS profile of the scalar field from two line sources positioned with y_{s_av}/h =1.0 and d/h = 1.50 is presented. Symmetry of the flow about the centreline is again verified.

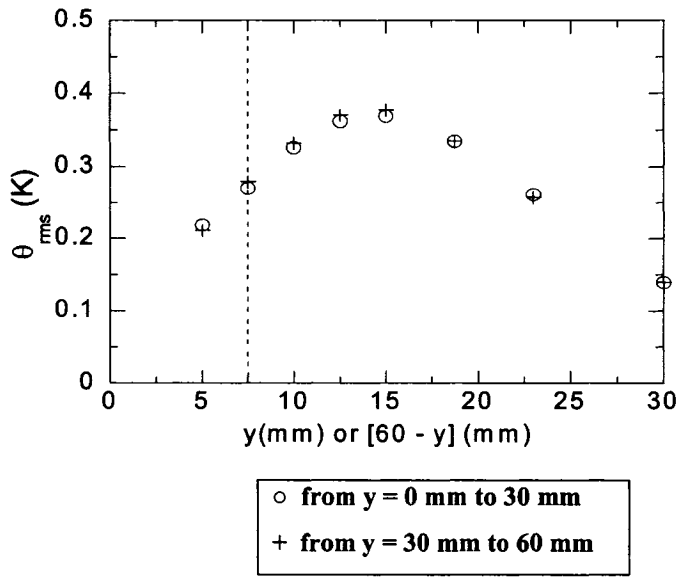

Figure 3.3 Symmetry test of θ_{rms} profile at x/h = 10.8 for line sources with y_{s_av}/h = 1.0 and d/h = 1.50. The line source positions are indicated by the vertical line.

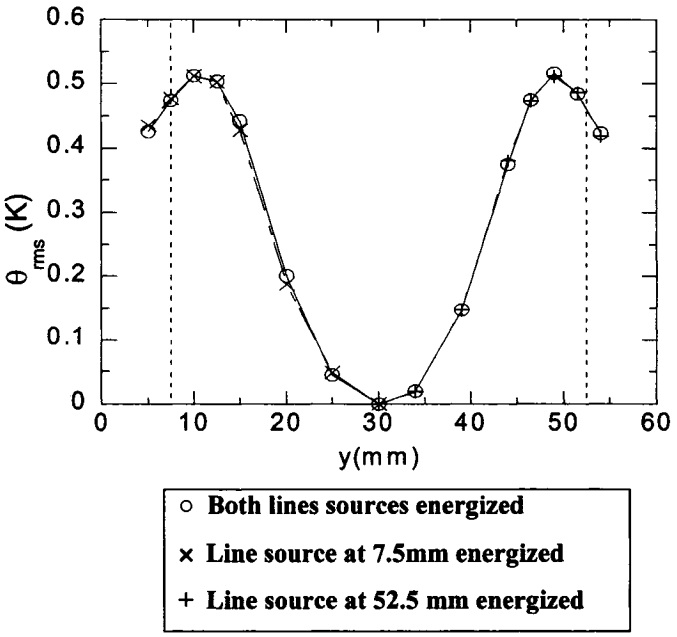

Figure 3.4 θ_{rms} profile at x/h = 4.0 for line sources with y_{s_av}/h = 1.0 and d/h = 1.50. Line source positions are indicated by vertical lines.

Lastly, Figure 3.4 shows the constancy of the power supply as required by the inference method (section 2.2.5). Therefore, in view of the presented results, the thermal field in the apparatus used meets all the experimental requirements.

3.2 Sources of error

The accuracy of most of the instruments and of the apparatus was discussed in Chapter 2. Three elements not yet considered are: errors in position estimates, electronic noise and error in measurement of the free-stream temperature.

There are two sources of positioning error. Firstly, the line source wall-normal distance has a maximum error of ± 0.15 mm positioning error. Secondly, the error in estimating the wall-to-probe distance is ± 0.20 mm. Thus the total positioning error in the wall-normal direction is ± 0.35 mm or ± 1.2 % of h.

As discussed in section 2.3, the measurements are low-pass and high-pass filtered. However, noise can be still present between the high-pass and the low-pass filter frequencies. To eliminate it from the measurements presented herein, the background thermal noise is measured before and after each experiment (i.e. the thermal field is measured in the same flow with the line sources turned off).

Experiments were only performed when the background RMS noise was less than 0.06 °C. If this was the case, the noise was subtracted from the measured signals on a mean-square basis, assuming that the signal and noise were uncorrelated (i.e. if $\theta_{measured} = \theta_{true} + \theta_{noise}$, $\langle\theta_{measured}^2\rangle = \langle\theta_{true}^2\rangle + \langle\theta_{noise}^2\rangle + 2\,\langle\theta_{true}\,\theta_{noise}\rangle$ and $\langle\theta_{true}^2\rangle = \langle\theta_{measured}^2\rangle - \langle\theta_{noise}^2\rangle$). The subtraction is done using a linear interpolation between the thermal noise measurements, assuming it varies linearly throughout the experiment. When removed, this operation represents a change of less than 1% for θ_{rms} measurements of 0.50 °C but 20 % for θ_{rms} measurements of 0.10 °C. The tails of a profile are therefore more affected by noise and less precise. This sometimes results in truncated profiles in chapter 4 when the noise prevails in the tails.

The final element is relevant to the mean upstream temperature measurements. The technique used to measure mean temperature is explained in section 2.2.3. The upstream temperature is not uniform and varies in time and position. This uneven profile can lead to measurement differences of up to 0.07°C between the thermistor reading and the probe in non-energized line source situations.

3.3 Flow properties

The experiments are performed at the following mean flow conditions. The centreline velocity is 5.2 m/s, the ambient temperature and pressure are nominally 21.5°C (varies between 20.0 °C and 23.0 °C) and 101 kPa. The kinematic viscosity (ν) is 1.53 x 10^{-5} m/s^2 and the Reynolds number under these conditions is 10200 (Re = Uh/ν).

Properties of the turbulence are of interest. The Kolmogorov scales are defined in section 2.2.4. To compute them, the dissipation of the turbulent kinetic energy (ε) is needed. The dissipation spectrum, which quantifies the dissipation at each wavenumber, is given by (Batchelor, 1953):

$$D(\kappa) = 2\nu\kappa^2 E(\kappa). \tag{3-5}$$

E(κ) is the three-dimensional energy spectrum and κ is the wavenumber. Following Tennekes & Lumley (1972):

$$\varepsilon = 2\nu\langle s_{ij}s_{ij}\rangle = \int_0^\infty D(\kappa)d\kappa = 2\nu\int_0^\infty \kappa^2 E(\kappa)d\kappa. \tag{3-6}$$

Expressing ε in terms of $E_{11}(\kappa_1)$, the one-dimensional longitudinal spectrum, the following relation is obtained assuming local isotropy (Hinze, 1959):

$$\varepsilon = 15\nu \int_0^\infty \kappa_1^{\,2} E_{11}(\kappa_1) d\kappa \,. \tag{3-7}$$

Taylor's hypothesis consists of considering the local flow as frozen in time when two measurements are taken over a short enough time interval. It is valid if the ratio u_{rms}/U_{mean} is small. A commonly accepted upper limit is 0.2 (Tennekes & Lumley, 1972). Assuming Taylor's hypothesis to be valid, the (longitudinal) wavenumber is related to frequency by:

$$\kappa_1 = \frac{2\pi f}{U} \,. \tag{3-8}$$

Consequently,

$$E_{11}(\kappa_1) = \frac{U}{2\pi} E_{11}(f) \tag{3-9}$$

and

$$\varepsilon = \frac{60\nu\pi}{U^2} \int_0^\infty f^2 E_{11}(f) df \,. \tag{3-10}$$

Following Tennekes & Lumley (1972), the integral scale is estimated as follows:

$$\ell = \frac{u_{rms}^3}{\varepsilon} \,. \tag{3-11}$$

Table 3.1 presents various turbulent flow properties at different y/h. As previously mentioned, the integral scale is of the order of h. The high level of dissipation and u_{rms} at the wall indicate that this is where most turbulence production occurs.

y/h	U (m/s)	u_{rms} (m/s)	ε (m^2/s^3)	ℓ(mm)	η (mm)	τ (ms)
0.033	2.81	0.60	7.02	30.77	0.150	1.48
0.100	3.73	0.48	5.50	20.10	0.160	1.67
0.167	4.06	0.42	4.11	18.01	0.172	1.93
0.267	4.37	0.39	3.15	18.83	0.184	2.20
0.333	4.48	0.36	2.19	21.31	0.201	2.65
0.500	4.73	0.32	1.24	26.36	0.232	3.51
0.667	4.99	0.27	0.91	21.70	0.251	4.12
0.833	5.15	0.22	0.64	16.74	0.274	4.90
1.000	5.20	0.19	0.57	12.05	0.282	5.18

Table 3.1 Flow properties

4. Results

In this chapter, the following results will be presented:

1. Scalar field statistical moments
2. Scalar correlation coefficient evolutions
3. Scalar co-spectra and coherency spectra

4.1 *Scalar field statistical moments*

For the subsequent analysis of the correlation coefficients and coherency spectra, statistical information contained in the temperature field is required. As one could expect, this represents large amount of data. Given that the main objective of this thesis is the study of the mixing of two scalars in turbulent channel flow, only selected results containing the important elements will presented in this section.

Figure 4.1 is a schematic of the experiment where the quantities y_{s_av}/h and d/h, the average distance of the line sources from the wall and the line source separation, respectively, are defined.

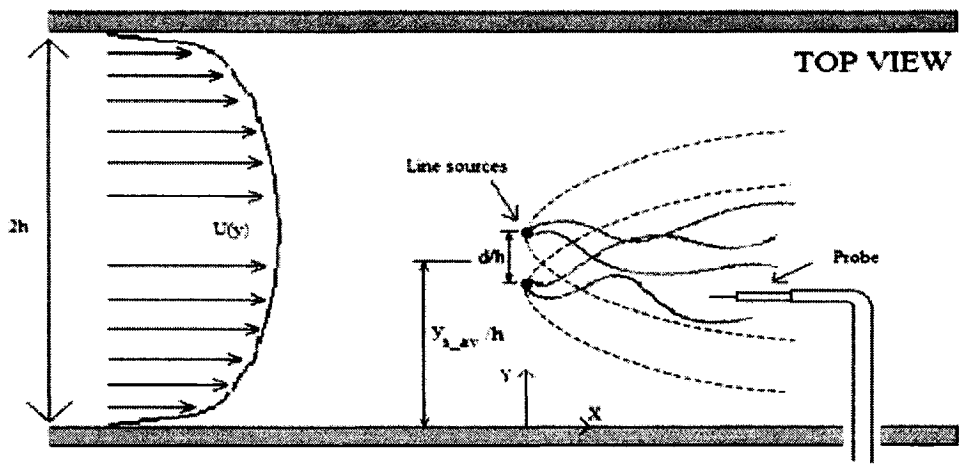

Figure 4.1 Schematic of the experiment. Solid line: instantaneous thermal wake. Dashed line: time-averaged wake. Modified from Vrieling & Nieuwstadt (2003).

From this point on, the following nomenclature is used to describe the different combinations of line source locations studied in this thesis:

		Average Position ($y_{s\ av}$/h)		
		0.2	0.5	1.0
Distance (d/h)	0.13	I	II	III
	0.27	IV	VI	VI
	0.50		VIII	IX
	1.50			VII

Table 4.1 Line source location nomenclature. Shaded combinations are not possible.

4.1.1 Mean temperature field

Mean temperature profiles for a single line source in turbulent channel flow were thoroughly discussed in Lavertu & Mydlarski (2005). They found that the transverse peak location of the mean profile stays at the line source position, y_s/h, for the range of x/h studied. The mean profiles were reasonably well approximated by truncated Gaussian distributions (Lavertu & Mydlarski, 2005), though their accuracy decreased with increasing downstream distance. Finally, the mean peak temperature excesses were found to decay as $x^{-0.7}$.

Mean temperature profiles behind two line sources can be deduced from the superposition of those produced by a single source. This is verified in Figure 4.2 and can be proved theoretically. Consequently, mean temperature profiles formed by multiple line sources can be obtained from the results of Lavertu & Mydlarski (2005) and are not discussed herein.

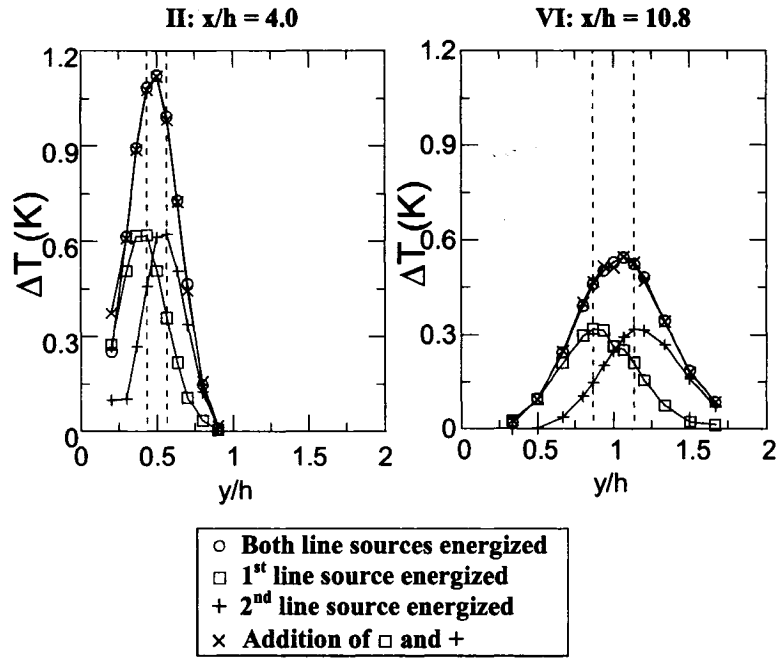

Figure 4.2 Typical transverse mean temperature profiles. The vertical lines are drawn at the locations of the line sources.

4.1.2 Fluctuating temperature field

Figure 4.3 presents the transverse normalized θ_{rms} profiles for the 9 combinations of line source locations. The θ_{rms} profiles depend on d/h, y_{s_av}/h and x/h. If the plumes are barely interacting (large d/h), then the θ_{rms} profiles are well separated and double peaks dominate. Double peaks in the θ_{rms} profiles emitted from two scalar sources were also observed in grid turbulence by Warhaft (1984) and in simulated turbulent channel flow by Vrieling & Nieuwstadt (2003).

At $y_{s\_av}/h = 0.2$, the accelerated merging of the thermal wakes for near-wall sources is linked to the presence of i) a boundary which concentrates the heat on one side of the line source, and ii) the higher TKE in this zone. Double peaks probably occur before x/h =4, since they were observed by Warhaft (1984) and Vrieling & Nieuwstadt (2003) early in the θ_{rms} downstream evolution. For combinations with $y_{s\_av}/h = 1.0$,

double peaks are present for a much longer time and for all d/h. The larger d/h cases are slower in merging their wakes and the double peaks are constantly present; in case VII some thermal wakes are clearly not interacting. Profiles with $y_{s\_av}/h = 0.5$ present hybrid characteristics; they start as double-peaked and become, at larger x/h, single peaked.

Double peaks in θ_{rms} profiles were also observed by Warhaft (1984) and Karnik & Tavoularis (1989) in homogeneous turbulence for single scalar sources and should not be confused with results using two sources. As Lavertu & Mydlarski (2005) have shown, single line source profiles in channel flow are not double peaked in the downstream domain studied in this thesis. Therefore, the presence of double peaks in Figure 4.3 is solely a consequence of the presence of two line sources.

It is also worth noting that the θ_{rms} peaks of combinations with $y_{s\_av}/h = 0.2$ and 0.5 move towards the channel centreline. This peak movement was observed using single line sources in Lavertu & Mydlarski (2005). They showed that the displacement rate of the peaks is a function of the line source location; the closer to the wall, the faster the displacement. In the present case, the movement also slows down as the peak moves towards the centreline.

The experiments performed for present work generated many single-line-source fluctuating temperature field results. Their normalized θ_{rms} transverse profiles can be found in the Appendix.

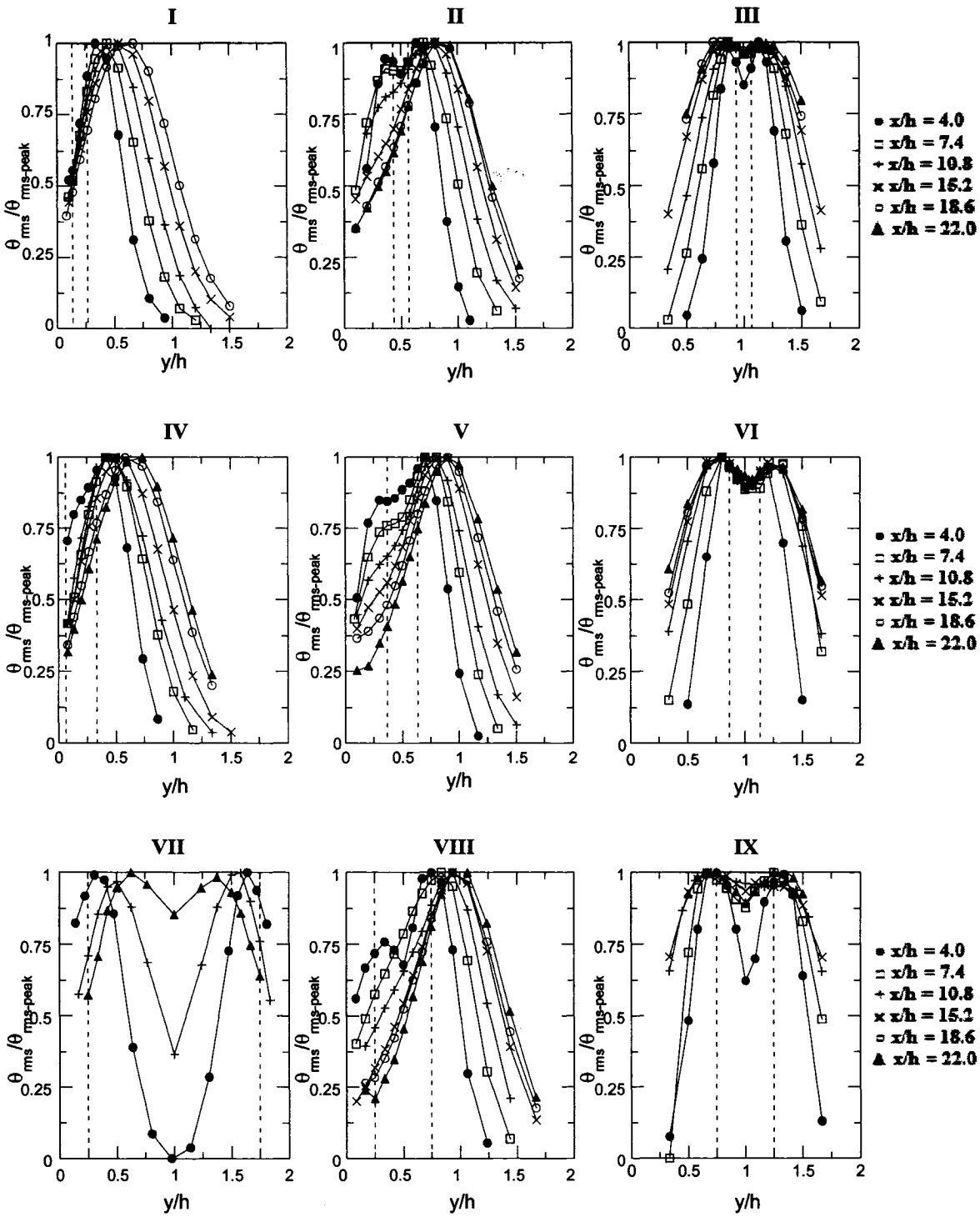

Figure 4.3 Transverse normalized θ_{rms} profiles for 9 combinations of line source locations. The vertical lines are drawn at the locations of the line sources.

It has been observed that the peak of the θ_{rms} profiles ($\theta_{rms\text{-}peak}$) generated by a single line source in different turbulent flows follows a power law decay in x: $\theta_{rms\text{-}peak} \propto x^n$. Figure 4.4 presents the downstream evolution of $\theta_{rms\text{-}peak}$ for the 9 combinations. It was found that the decay is proportional to n = -0.9 when only one line source is energized, consistent with the results of Lavertu & Mydlarski (2005) for a single line source in channel flow. In homogeneous turbulent shear flow, Karnik & Tavoularis (1989) found two regimes using a single line source, one having n = -0.85 and the other having n = -1.7. Warhaft (1984) found, in isotropic turbulence, a value of n = -0.8 for $\frac{x_o}{M} \geq 3$.

In cases where the level of interaction between the thermal wakes is very small, the two-line-source $\theta_{rms\text{-}peak}$ behaves like the single-line-source $\theta_{rms\text{-}peak}$ and its decay exponent is equal to that of a single line source. This is true for cases VII and IX in Figure 4.4. However, when the level of interaction is significant, the decay of the peak of θ_{rms} profiles for two line sources is less accurately described by a power law. The $\theta_{rms\text{-}peak}$ value is therefore dependent on the scalar covariance.

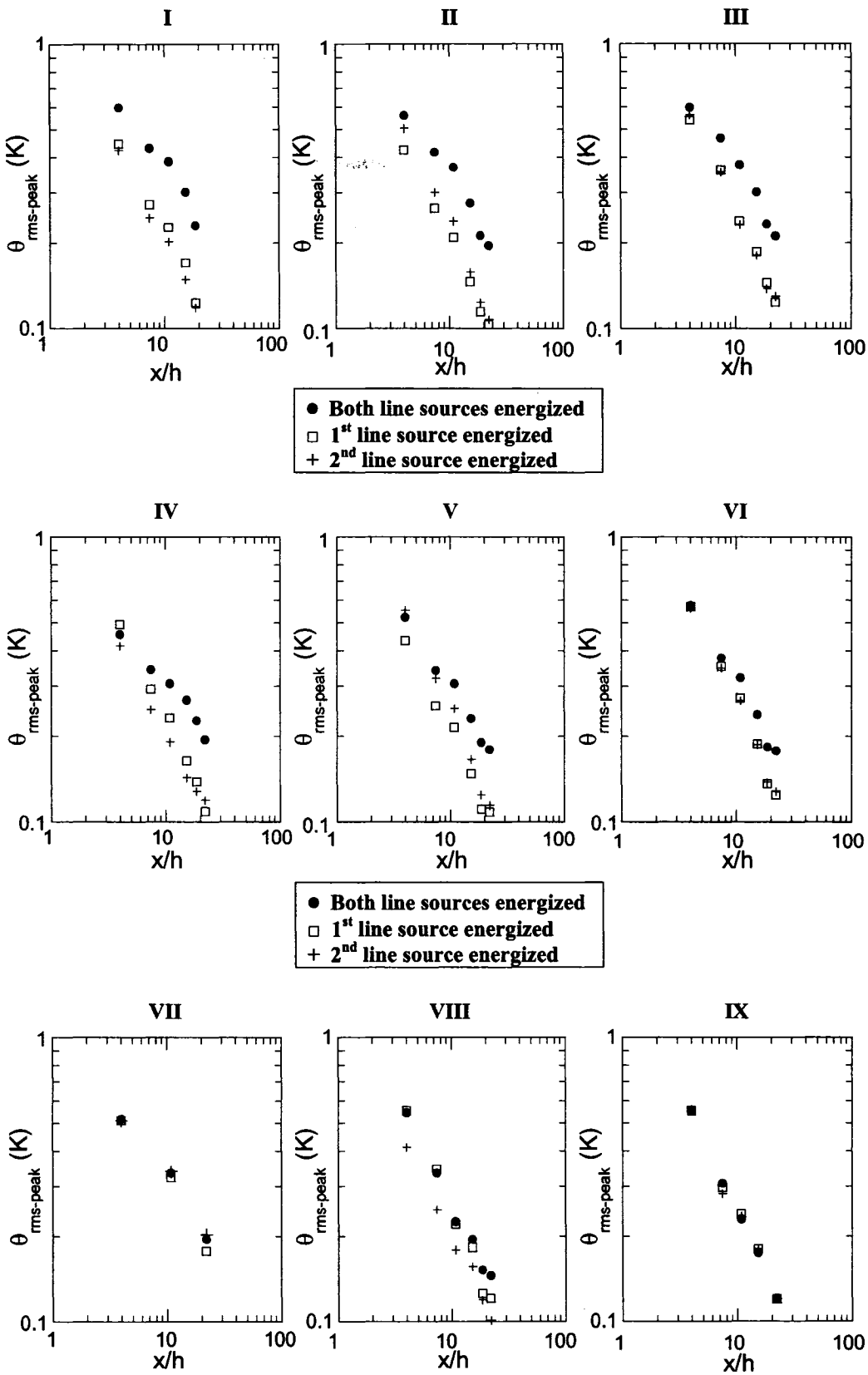

Figure 4.4 Downstream evolution of the peak θ_{rms} for 9 combinations of line source locations.

Figure 4.5 shows selected θ_{rms} profiles with two line sources energized as well as each line source energized independently. It is clear from Figure 4.5 that the θ_{rms} profile for both line sources energized cannot be directly obtained from the addition of single line source data and that the covariance is an important parameter.

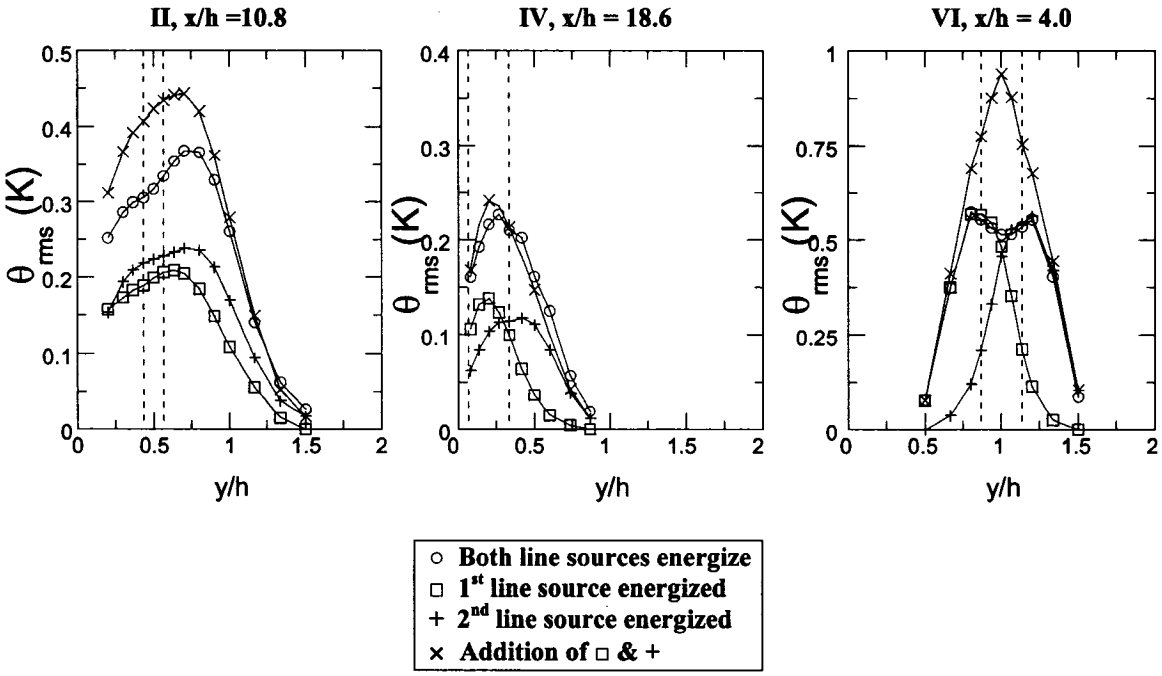

Figure 4.5 Typical transverse θ_{rms} profiles

4.2 Scalar correlation coefficient evolutions

The temperature correlation coefficient (ρ) is used to describe the mixing process and is the non-dimensional form of the covariance $\langle\theta_1\theta_2\rangle$. The correlation coefficient rates the quality of the local mixing process whereas the covariance represents the total amount of local mixing. ρ can be high in a region where the quantities mixed locally are small.

In turbulent channel flow, ρ is a function of three parameters: the downstream distance (x/h), the separation between the line sources (d/h) and the average position of the line sources (y_{s_av}/h). As was the case in section 4.1.2 for θ_{rms}, all three variables should affect the evolution of the covariance.

In the region very close to the sources, there is no correlation as there is no overlapping of the plumes. $\langle\theta_{12}^2\rangle$ is therefore the sum of $\langle\theta_1^2\rangle + \langle\theta_2^2\rangle$ ($\rho = 0$). Far downstream of the line sources, the correlation coefficients asymptote to 1 (Tong & Warhaft, 1995) — the thermal wakes are perfectly mixed. Thus, ρ goes from 0 to 1 in its downstream evolution. However the (non-monotonic) transition between these two limits is a function of the flow.

In the downstream evolution, two zones can be distinguished. Firstly, there is a zone of negative gradient in ρ, where the wakes are not instantaneously overlapping. In this zone, the gradient is negative because ρ evolves from unmixed ($\rho = 0$) at $x/h = 0$ to its most anti-correlated point. Then, as the plumes widen and the overlap increases, the probe measures in both wakes more frequently and the gradient of ρ becomes positive and ρ tends towards 1.

The evolution is controlled by two mixing mechanisms: wake flapping and internal turbulent mixing. Both are caused by the turbulent nature of the flow, but are different in the length (and time) scales of the flow they impact upon. The former is dominant early in the downstream evolution and is characterized by the bulk displacement of the thermal plumes. It is a large-scale phenomenon. Integral-size eddies move the thermal plumes to the right or left side of the channel, thus helping them widen their time-averaged thermal wake and mix. Flapping is present throughout the downstream evolution but diminishes in relative importance as the thermal wakes widen.

Internal turbulent mixing is done by eddies of various size contained within the thermal plumes. They mix energy rapidly in the plumes, more so than by wake flapping. When the overlap zone is large and constant, internal turbulent mixing is effective in blending the thermal wakes. It increases in importance further downstream, when the wake flapping decreases.

4.2.1 Transverse profiles

The transverse profiles of ρ at different downstream positions for the 9 source combinations are shown in Figure 4.6. The correlation coefficient is very sensitive to minor changes in the θ_{rms} values. Repetition of the experiments showed that a precision of $\pm$ 0.05 in ρ is obtained. If there is no ρ profile for a given x/h in Figure 4.6, this implies that ρ is equal to 0 or 1. Most profiles exhibit a (relative) minimum value of ρ in the region between the two line sources, and a maximum value in the tails of the profile. However, this is not generally the case for the range of measurements herein when both sources are located close to a wall. In this case, ρ increases from the wall towards y/h = 2.0.

From an instantaneous point of view, the thermal wakes are not continuously present in the tails of the θ_{rms} profiles. Occasionally a large eddy carries part of the plumes there. When the two line sources are close together, a large eddy, moving both plumes simultaneously, causes the large values of ρ in the tails of the profiles.

The presence of a minimum ρ value close to y_{s_av}/h is due to measurements taking place in one wake and then in the other. Early downstream, as Warhaft (1984) explained, when the two line sources are close together, integral-size eddies move both thermal wakes simultaneously in the same direction and no instantaneous overlapping of the wakes exists. This leads to a negative correlation coefficient. Both the minimum in between the sources and the high ρ in the tails were observed by Warhaft (1984) and Tong & Warhaft (1995).

The minimum ρ for combinations centered at $y_{s\_av}/h = 0.2$ & 0.5 moves towards the wall with increasing x/h. A movement of the minimum ρ towards the jet centreline was observed by Tong & Warhaft (1995). These phenomena may be related to the fact that, in both cases, the minimum is moving towards a region of high TKE and, in turbulent channel flow, towards a zone where flapping is less important (due to presence of the wall). With increasing downstream distance, the internal turbulent mixing increases and the ρ profiles flatten.

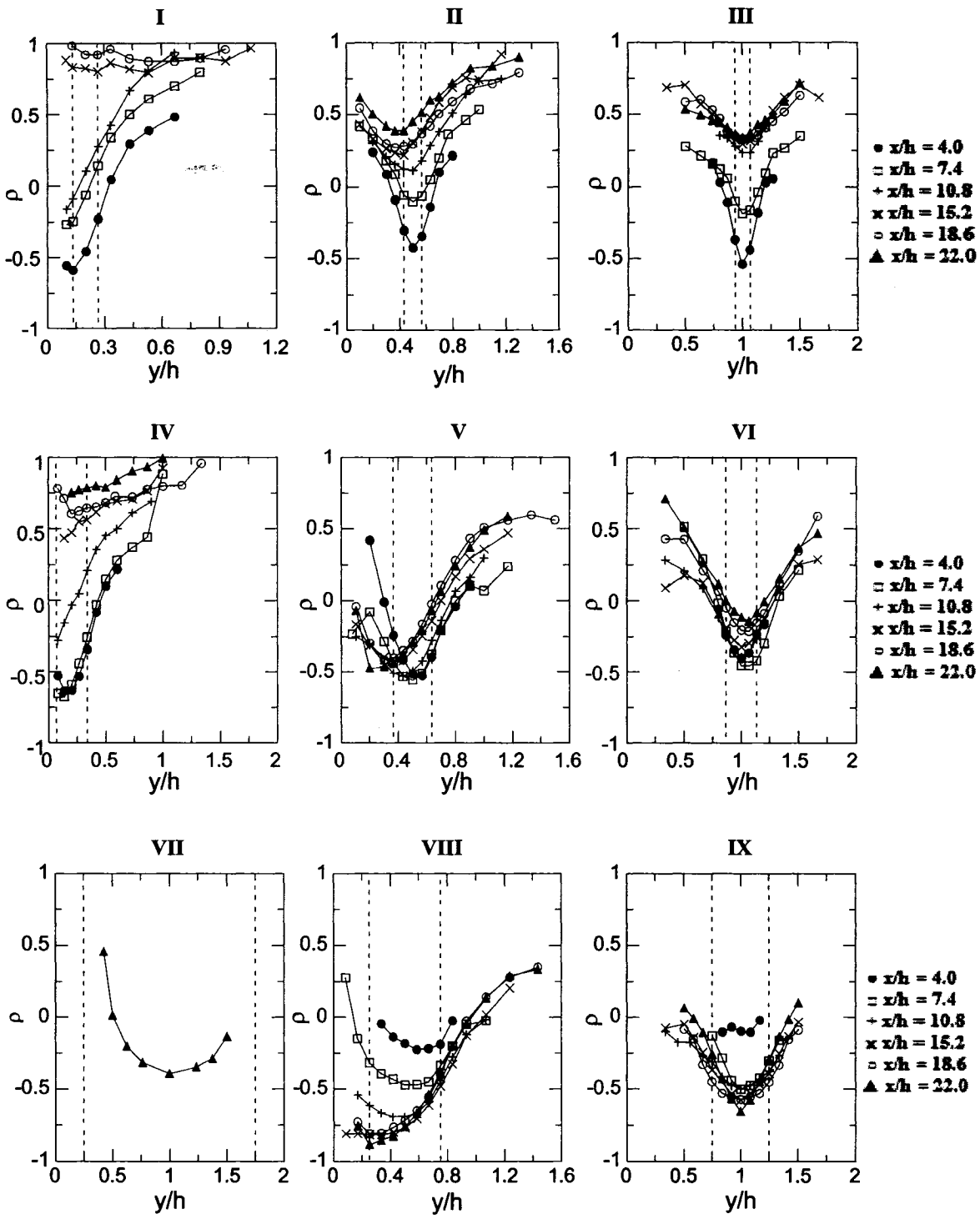

Figure 4.6 Transverse profiles of ρ for 9 combinations of line sources locations. The vertical lines are drawn at the locations of the line sources.

4.2.2 Evolution of ρ_{min} and $\rho_{ys\_av/h}$

To compare the evolution of different combinations, both the minimum value of ρ (ρ_{min}) measured in the transverse profile and ρ evaluated at $y = y_{s\_av}/h$ ($\rho_{ys\_av/h}$) will be studied. The latter was used by Warhaft (1984) and Tong & Warhaft (1995) in their analyses. From an engineering point of view, the minimum value of ρ will be an especially important quantity. It can be used to determine the minimum possible quality of mixing for a given situation.

Figures 4.7 and 4.8 show the evolution of ρ with respect to x/h for a given d/h with different y_{s_av}/h. Up to x/h = 7.4, ρ is approximately independent of y_{s_av}/h for a given d/h. For x/h > 7.4, combinations with $y_{s\_av}/h = 0.2$ rapidly increase towards ρ = 1. Such jumps were also seen by Tong & Warhaft (1995) in similar situations. Also, from this point on, the combinations with $y_{s\_av}/h = 1.0$ have higher ρ than the ones with $y_{s\_av}/h = 0.5$. It is also observed that profiles having a d/h = 0.50 start at ρ = 0 and continuously decrease; they are still in the first part of their development and the downstream domain is too short to observe their rise towards positive ρ.

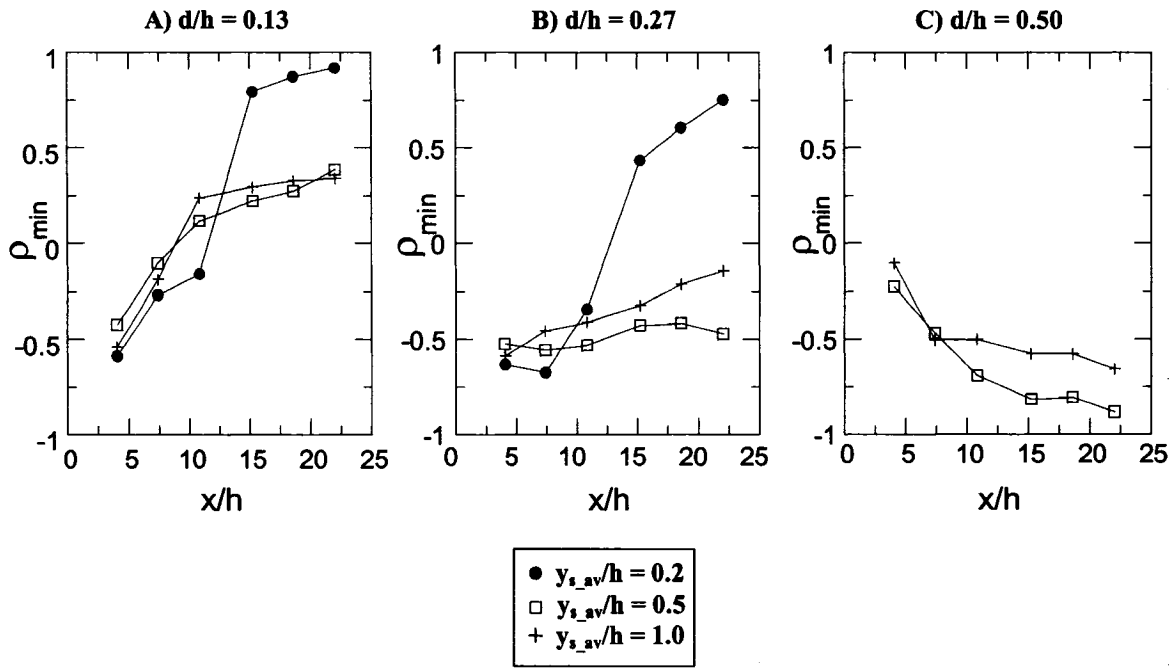

Figure 4.7 Evolution of ρ_{min} with respect to the downstream position (x/h) for different average source positions (y_{s_av}/h).

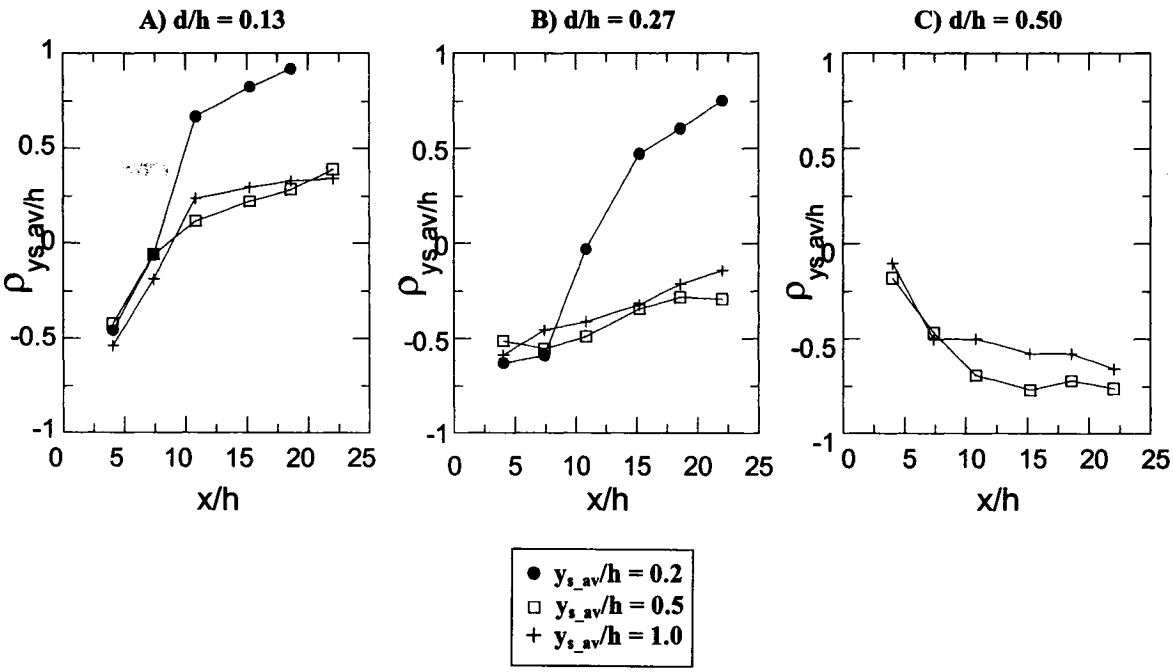

Figure 4.8 Evolution of $\rho_{ys\_av/h}$ with respect to the downstream position (x/h) for different average source positions (y_{s_av}/h).

The evolution of ρ with respect to x/h for a given y_{s_av}/h with different d/h is plotted in Figures 4.9 and 4.10. Graph C) in both figures is the same because $\rho_{min} = \rho_{ys\_av/h}$ when $y_{s\_av}/h = 1.0$. It is clear from these figures that the closer the line sources (small d/h), the faster the correlation coefficient approaches its asymptotic limit of 1. Small d/h allows internal turbulent mixing to occur sooner as the thermal plumes will overlap more rapidly. Similarly to Figures 4.7 and 4.8, Figures 4.9 and 4.10 show that, early downstream, d/h is a more important factor than y_{s_av}/h. Early downstream, the mixing resembles that in grid turbulence, where ρ is only a function of the separation distance between the line sources and the downstream position (Warhaft, 1984).

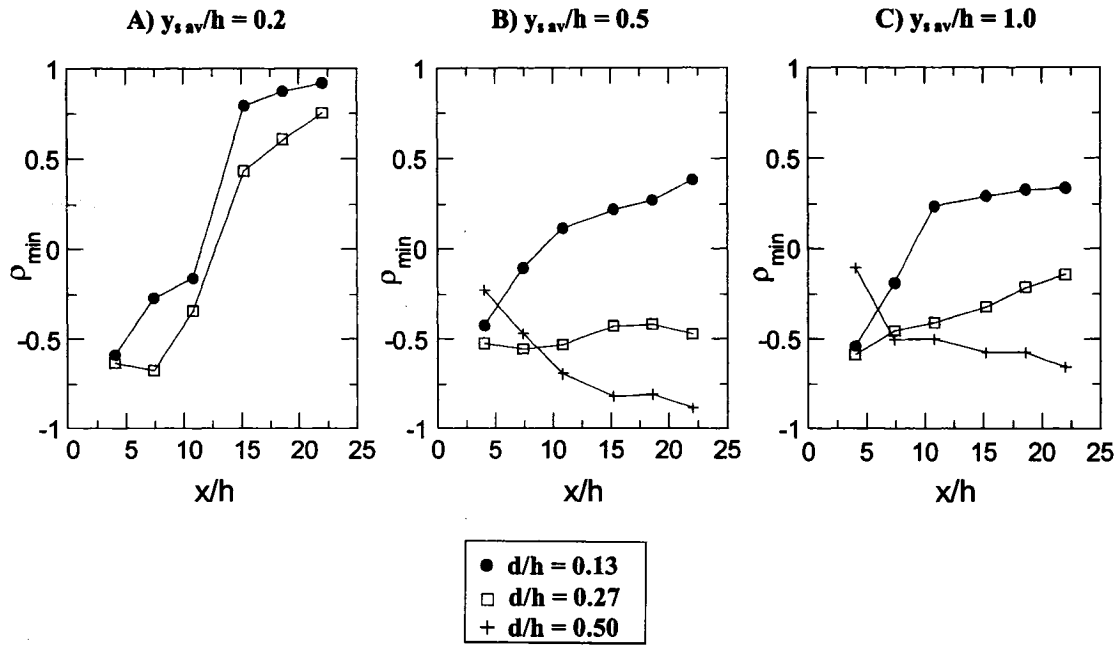

Figure 4.9 Evolution of ρ_{min} with respect to the downstream position (x/h) for different source separations (d/h).

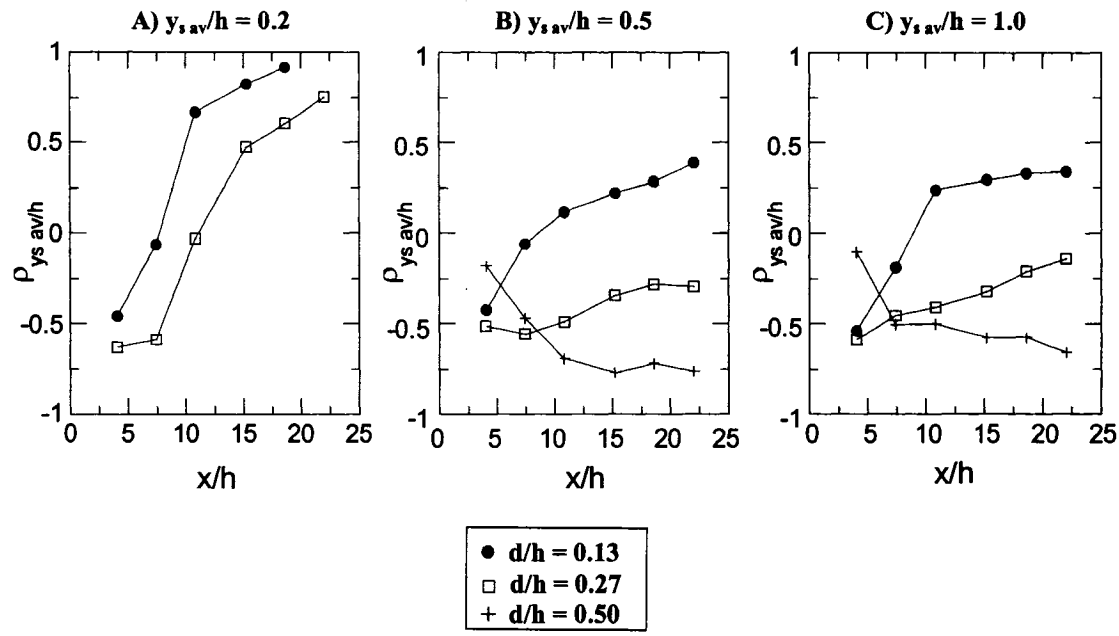

Figure 4.10 Evolution of $\rho_{ys\_av/h}$ with respect to the downstream position (x/h) for different source separations (d/h).

Figures 4.11 and 4.12 plot ρ_{min} and $\rho_{ys\_av/h}$ as a function of y_{s_av}/h. It is observed that the combinations with $y_{s\_av}/h = 0.2$ separate themselves from the others around $x/h \approx 10.0 - 15.0$. It appears that the high turbulence intensity at the wall rapidly increases ρ for combinations with $y_{s\_av}/h = 0.2$ through increased turbulent mixing near the wall. This does not affect other combinations with larger y_{s_av}/h as they are too far from the wall.

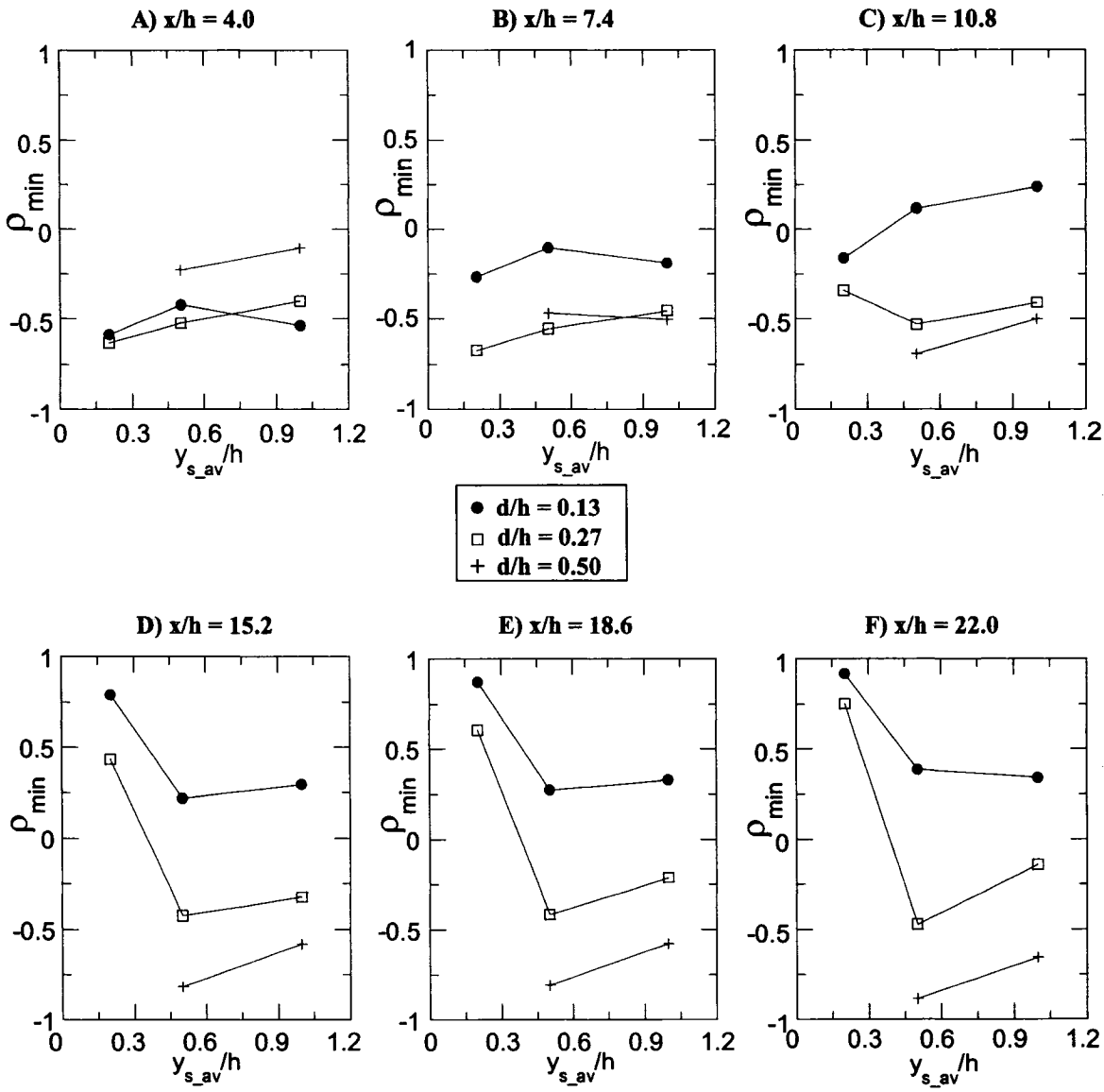

Figure 4.11 Evolution of ρ_{min} with respect to the average position of the line sources (y_{s_av}/h) for different source separations (d/h).

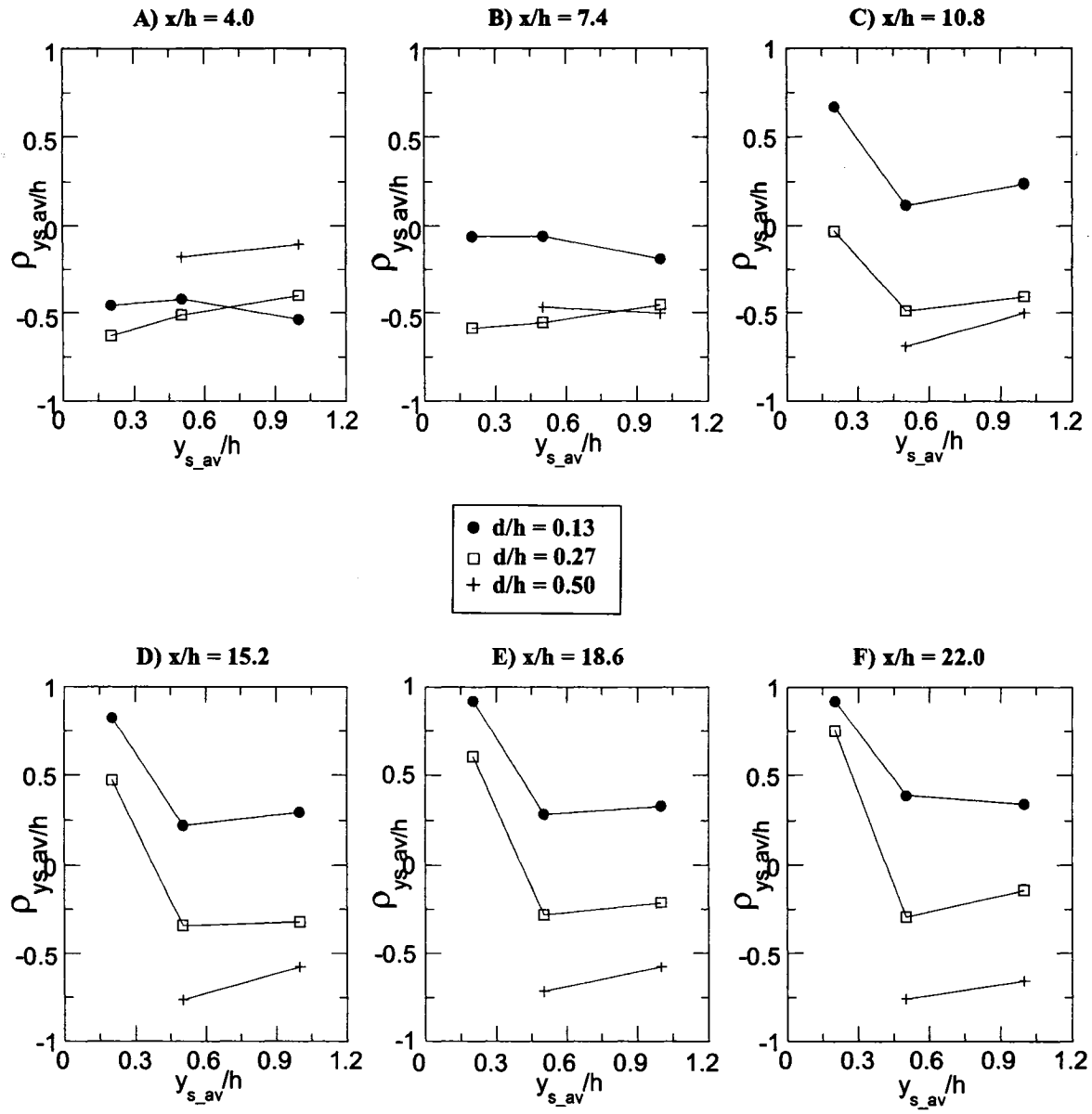

Figure 4.12 Evolution of $\rho_{ys\_av/h}$ with respect to the average position of the line sources (y_{s_av}/h) for different source separations (d/h).

Figures 4.13 and 4.14 plot ρ_{min} and $\rho_{ys\_av/h}$ as a function of d/h. As x/h increases, the results for the smallest separation (d/h = 0.13) increase more rapidly. Furthermore, the previously observed jump in ρ for sources with $y_{s\_av}/h = 0.2$ is also observed in these figures. d/h is clearly an important factor.

It is also observed that the results with $y_{s\_av}/h = 0.5$ and 1.0 behave in a similar manner. ρ is generally higher with $y_{s\_av}/h = 1.0$ than with $y_{s\_av}/h = 0.5$. This is presumably due to the higher levels of mixing by wake flapping which are present for $y_{s\_av}/h = 1.0$.

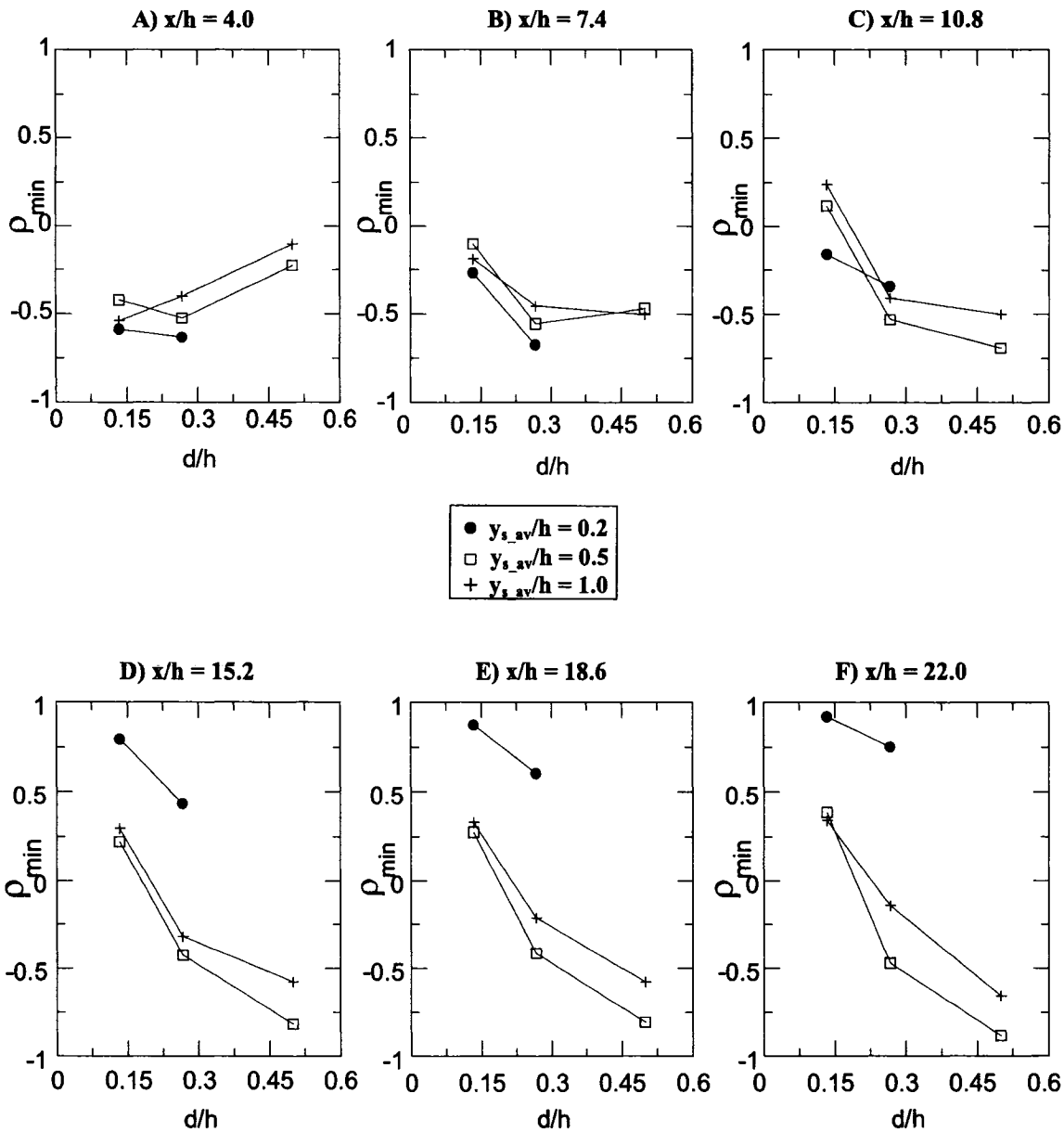

Figure 4.13 Evolution of ρ_{min} with respect to the distance between line sources (d/h) for different average source positions (y_{s_av}/h).

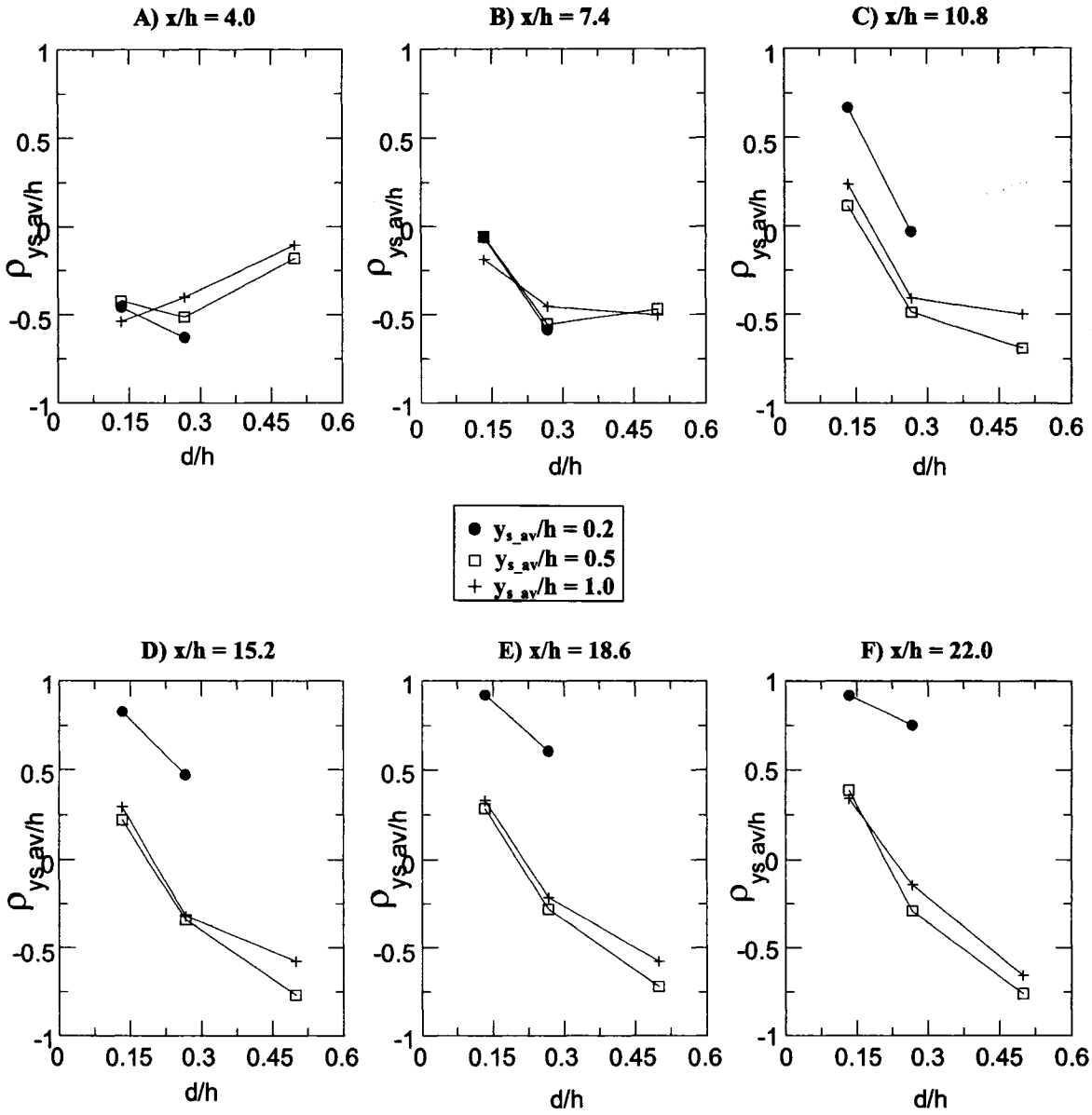

Figure 4.14 Evolution of $\rho_{y_{s\_av}/h}$ with respect to the distance between line sources (d/h) for different average source positions (y_{s_av}/h).

Differences between ρ_{min} and $\rho_{ys\_av/h}$ are highlighted in Figure 4.15. Firstly, for $y_{s\_av}/h = 0.5$, with $d/h = 0.13$, ρ_{min} and $\rho_{ys\_av/h}$ are identical to within the experimental error. For $d/h = 0.27$ & 0.5, the difference is larger and grows as x/h increases. Clearly, for the latter two d/h, the increasing distance between ρ_{min} and $\rho_{ys\_av/h}$, as seen in Figure 4.6, leads to differences as high as $\Delta\rho = 0.2$ for $y_{s\_av}/h = 0.5$.

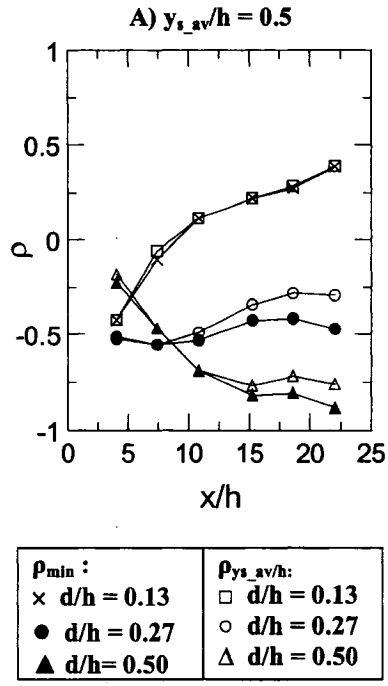

Figure 4.15 Comparison of ρ_{min} and $\rho_{ys\_av/h}$

4.2.3 Comparisons with previous research

As discussed in section 1.2.4, Warhaft (1984) was able to collapse the evolutions of ρ for the mixing of two scalars in isotropic turbulence. The correlation coefficient in isotropic turbulence was shown to be a function of two parameters, $\frac{d}{\ell}$ and $\frac{x}{d}\frac{v}{U}$. Figures 4.7 and 4.8 showed the dominance of d/h in the mixing early downstream. Thus, some ρ evolution profiles appear similar to those in grid turbulence. It must be noted that this simplification only holds at best for ρ_{min} and $\rho_{ys\_av/h}$. The evolution of the ρ profiles presented in Figure 4.6 is clearly dependent on d/h, y_{s_av}/h and x/h at all times.

Figure 4.16 presents an attempt to collapse the ρ_{min} evolutions with $y_{s\_av}/h = 0.5$ & 1.0 using Warhaft's (1984) non-dimensionalization. In $\frac{x}{d}\frac{v}{U}$, where v is the fluctuating RMS velocity in the wall-normal direction, $\frac{x}{U}$ represents the time from scalar insertion to probe measurement and $\frac{d}{v}$ is the lateral convective timescale. v values were determined using the results of Kim et al. (1987). As shown in Figure 4.16, Warhaft's (1984) non-dimensionalization does not eliminate the y_{s_av}/h dependence between $y_{s\_av}/h = 0.5$ & 1.0. It is possible that a more complex non-dimensionalization could accurately collapse the present data, however, none was discovered.

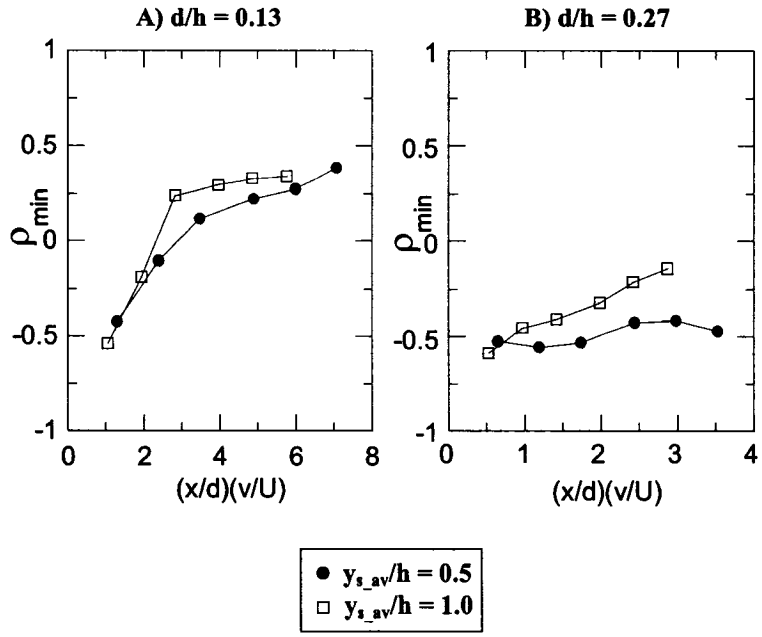

Figure 4.16 Non-dimensionalized evolution of ρ_{min}

Another possible parallel between grid turbulence and turbulent channel flow would be that for combinations with $y_{s\_av}/h = 1.0$, $\rho_{ys\_av/h}$ would share an equivalent evolution (up to a certain downstream distance) given that turbulent channel flow is almost homogeneous around y/h = 1.0. This assumption was used by Vrieling &

Nieuwstadt (2003) to compare their simulations with published experimental results (Warhaft, 1984).

Figure 4.17 shows the downstream evolution of $\rho_{ys\_av/h}$ in grid turbulence (Warhaft, 1984) and in a turbulent jet (Tong & Warhaft, 1995). The latter turbulence is inhomogeneous and decaying, and is thus more complex than grid turbulence (or turbulent channel flow). The separation of the scalar sources in grid turbulence is given by d/M, where M is the mesh size, and, in a turbulent jet, by r_{s_av}/D and d/D, where D is the jet diameter.

In view of Figure 4.8 and Figure 4.17, one can conclude that, in turbulent channel flow, $\rho_{ys\_av/h}$ with $y_{s\_av}/h = 1.0$ evolves in a similar manner to $\rho_{ys\_av/h}$ in grid turbulence for smaller downstream distances. At large d/h, ρ decreases in grid turbulence and turbulent channel flow. Tong & Warhaft (1995) have shown that in a turbulent jet, ρ reaches one faster than in grid turbulence. This is also the case for turbulent channel flow, and especially for $y_{s\_av}/h = 0.2$, where the high turbulence intensity near the wall leads to faster mixing.

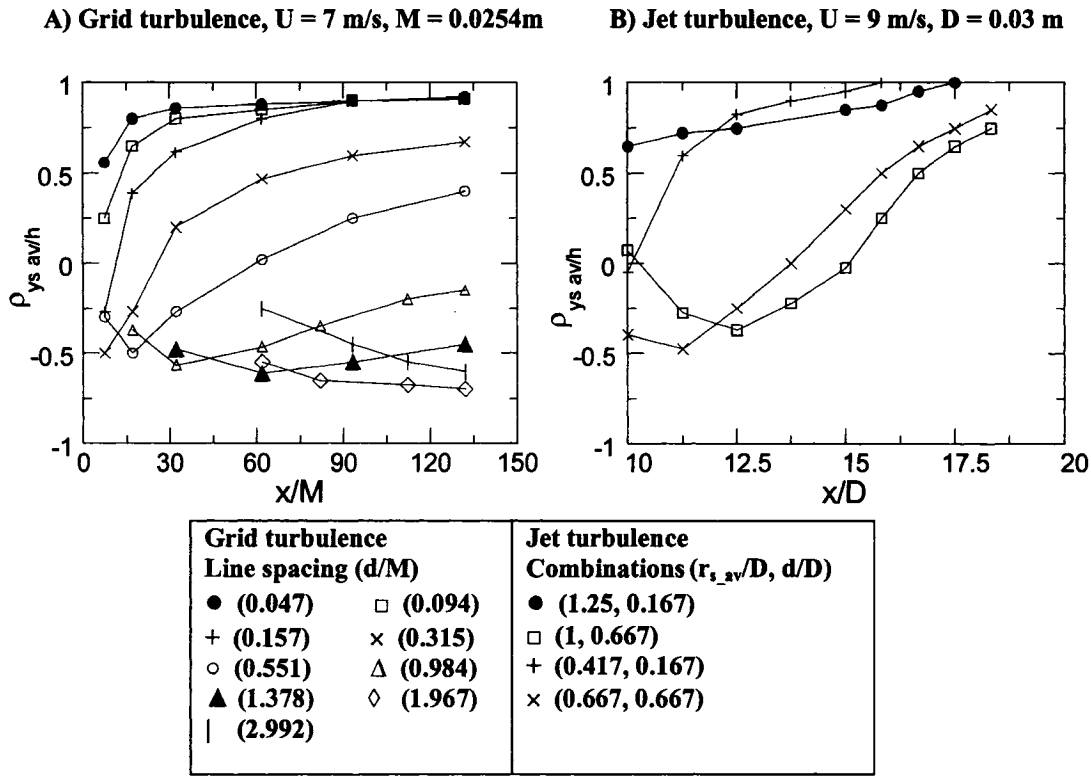

Figure 4.17 Downstream evolution of ρ for different flows. In grid turbulence, the line sources are located at x/M = 20. In turbulent jet, the ring sources are located at x/D = 9.

4.3 Scalar co-spectra and coherency spectra

The study of mixing by means of spectral analysis is a powerful tool as it gives information about the mixing at different scales. In this section, cases II, IV and IX — a representative selection of the studied combinations — were analyzed. Figures 4.18, 4.19, 4.20 and 4.21 show their co-spectra and their coherency spectra, as defined in section 1.1.2. These spectra are plotted as a function of $\kappa\eta$, where κ is the wavenumber and η the Kolmgorov microscale. Consequently, $\kappa\eta = 1$ at the Kolmogorov microscale. The co-spectra are non-dimensionalized by dividing by the peak of the θ_{rms} profiles behind single line sources and multiplying by the frequency such that the integral of the resulting co-spectrum is a non-dimensional covariance.

As can be seen from Figures 4.18 – 4.21, most of the production of covariance (negative or positive) is contained between $\kappa\eta = 0.01$ and $\kappa\eta = 0.1$ (10 to 100 times the Kolmogorov microscale). (The integral scales are approximately 100η.) As would be expected, the downstream evolution of the co-spectra follows the downstream evolution of the correlation coefficient. In other words, negative co-spectra occur when ρ is negative and similarly for positive co-spectra. The general trend towards positive covariance as $x/h \rightarrow \infty$ is clear from the figures.

The coherency spectrum (i.e., the non-dimensionalized co-spectrum) can be considered as a spectral correlation coefficient. It fluctuates around an approximate plateau for most scales, when the line sources are far from the wall (Figures 4.18, 4.19 4.21). The mean value corresponds to the correlation coefficient for the same case.

In the absence of the high turbulence intensities associated with near-wall turbulence, the degree of mixing is approximately uniform in most of the spectral domain. Near the wall (case IV, Figure 4.20), the high turbulence intensity results in a noticeable variation in the coherency across the scales. The large-scale coherency changes much faster than that of the small scales. Given that turbulence production is a large-scale phenomenon, its effect is probably first felt at low wavenumbers. It will only be felt at the smaller scales after enough time has passed for the mixing to be transferred on to the smaller scales. A coherency spectra evolution similar to case IV (i.e. fast movement at the large scales and slower at smaller scales) was also observed by Tong & Warhaft (1995) for two scalar sources in a turbulent jet.

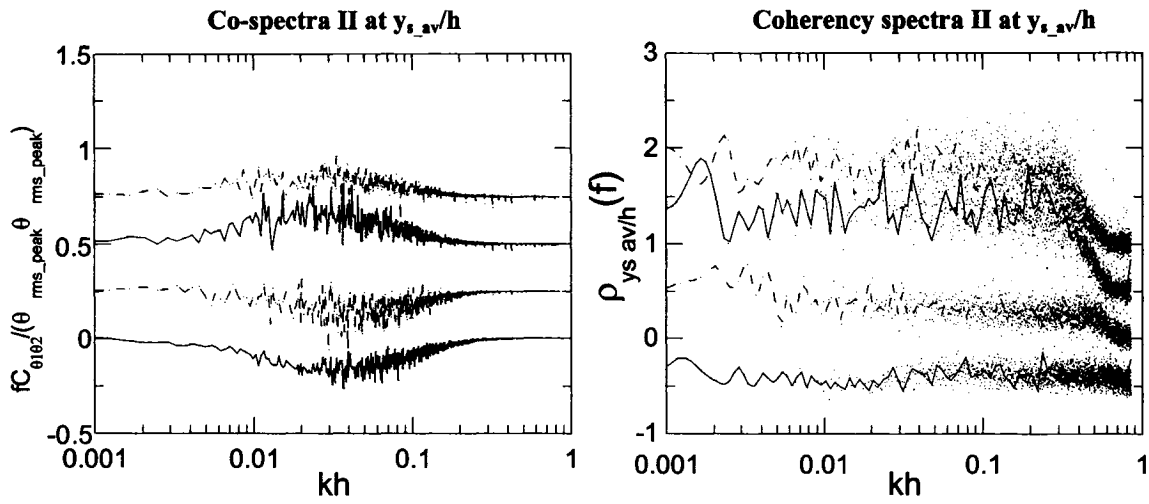

From bottom to top:	Co-spectra: Each curve has been shifted up by 0.25 with respect to the previous curve.
1st line x/h = 4.0	
2nd line x/h = 7.4	
3rd line x/h = 15.2	Coherency spectra: Each curve has been shifted up by 0.50 with respect to the previous curve.
4th line x/h = 18.6	

Figure 4.18 Co-spectra and coherency spectra for case II (y_{s_av}/h = 0.5, d/h = 0.13) measured at $y = y_{s\_av}/h$.

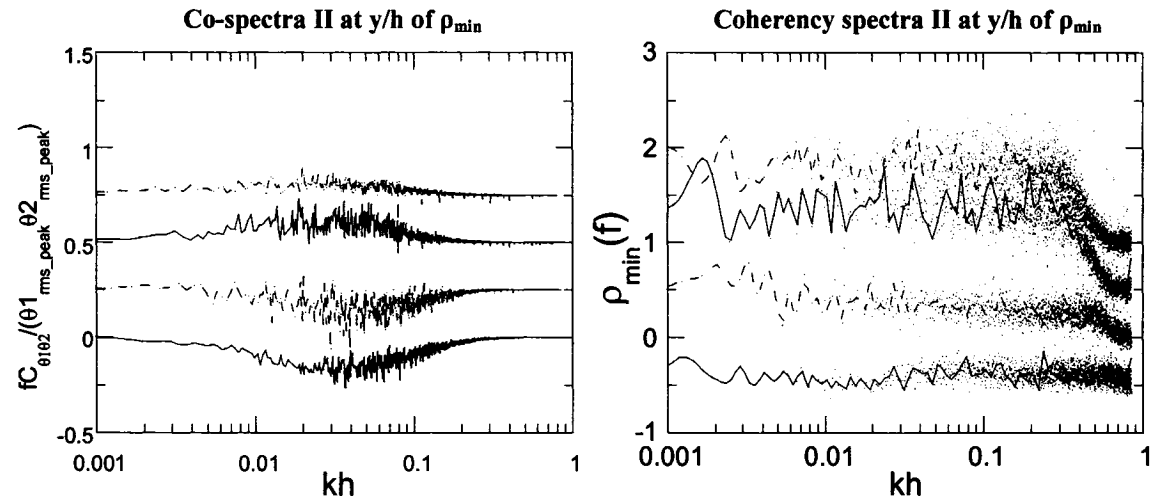

From bottom to top:	Co-spectra: Each curve has been shifted up by 0.25 with respect to the previous curve.
1st line x/h = 4.0	
2nd line x/h = 7.4	
3rd line x/h = 15.2	Coherency spectra: Each curve has been shifted up by 0.50 with respect to the previous curve.
4th line x/h = 18.6	

Figure 4.19 Co-spectra and coherency spectra for case II (y_{s_av}/h = 0.5, d/h = 0.13) measured at the y/h corresponding to ρ_{min}.

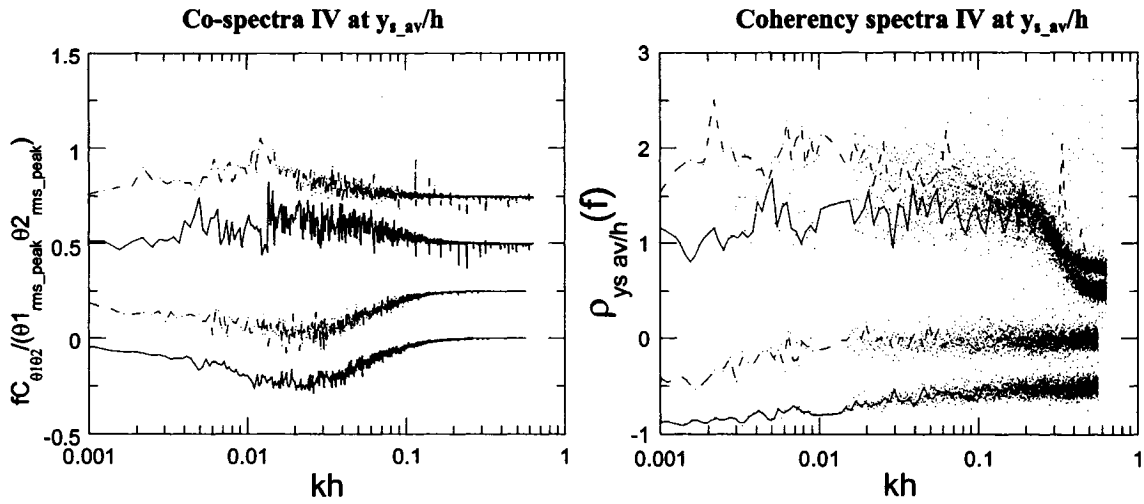

From bottom to top:	Co-spectra: Each curve has been shifted up by 0.25 with respect to the previous curve.
1st line x/h = 4.0	
2nd line x/h = 7.4	
3rd line x/h = 15.2	Coherency spectra: Each curve has been shifted up by 0.50 with respect to the previous curve.
4th line x/h = 18.6	

Figure 4.20 Co-spectra and coherency spectra for case IV ($y_{s\_av}/h = 0.2$, $d/h = 0.27$) measured at $y = y_{s\_av}/h$.

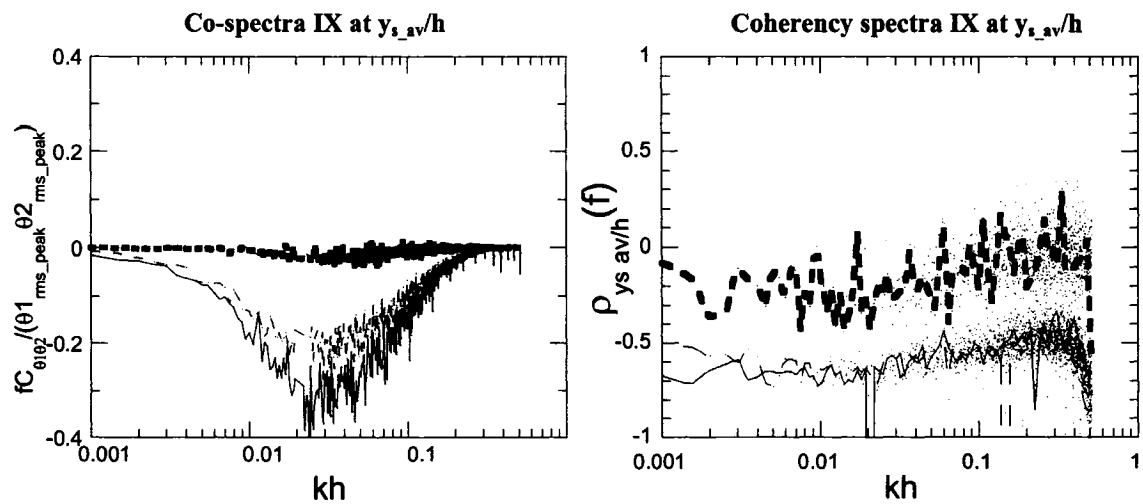

Thick dotted line x/h = 4.0
Solid line x/h = 7.4
Dotted line x/h = 15.2

Figure 4.21 Co-spectra and coherency spectra for case IX ($y_{s\_av}/h = 1.0$, $d/h = 0.5$) measured at $y = y_{s\_av}/h$.

5. Conclusions

The objective of this work was to study the mixing of two scalars in turbulent channel flow and, more specifically, to analyze the evolution and interaction of two thermal fields released from concentrated sources. To this end, 9 combinations of source locations were studied at 6 different downstream distances for a total of 54 sets of measurements. Transverse profiles of i) the mean excess temperature, ii) the RMS temperature fluctuations, and iii) the correlation coefficient were studied. Typical co-spectra and coherency spectra of the two temperature fields were also measured.

It was shown that the mean excess temperature profiles could be deduced from those emitted from a single source. However, the additive nature of the mean excess temperature profiles emitted from two line sources was not exhibited by the corresponding θ_{rms} profiles, which were therefore studied in detail. They were found to depend on three parameters: i) the separation distance between the line sources (d/h), ii) their average wall normal position (y_{s_av}/h), and iii) the downstream position (x/h) of the measurement probe.

The transverse θ_{rms} profiles produced by two sources revealed some similarities with those emitted from one source. For example, the peak of the θ_{rms} profiles drifted towards y/h = 1.0 for line sources with y_{s_av}/h = 0.2 and 0.5. Furthermore, the peak of the θ_{rms} profiles emitted from two sources decayed with increasing downstream distance. Many differences also existed. Some of the transverse profiles exhibited double peaks in the early stages of their evolution. Double peaks were the most persistent for source locations with y_{s_av}/h = 1.0 (where flapping of the thermal wakes was most prominent and internal turbulent mixing the weakest). They were the least common for sources located with y_{s_av}/h = 0.2 (where flapping of the wakes was the weakest and turbulent mixing the strongest). In addition, the downstream decay of the peaks of the measured θ_{rms} profiles was not well represented by a power law (excluding situations where the two wakes had not yet interacted), unlike θ_{rms} profiles emitted from one source.

The correlation coefficient was used to evaluate the mixing of the two scalars. It represents the non-dimensionalized covariance – a measure of the efficiency of the mixing process. However, it should be noted that only the (dimensional) covariance dictates the total (or absolute) amount of mixing. Therefore, large correlation coefficients do not always imply high levels of mixing, whereas large covariances, which inevitably lead to large correlation coefficients, always imply high levels of mixing. (The dimensional covariance profiles can be inferred from the correlation coefficient profiles and the single-line-source θ_{rms} profiles found in the Appendix.)

The transverse profiles of the correlation coefficient (ρ) were also found to depend on d/h, y_{s_av}/h, and x/h. The correlation coefficient must initially be zero (at x/h=0) and must asymptote to 1 (as $x/h \rightarrow \infty$). This evolution is non-monotonic and ρ is initially negative due to the early dominance of flapping of the thermal wakes by turbulent eddies (before the former have widened significantly). Consequently, the downstream domain was too short to observe the correlation coefficient profiles' tendency tend towards perfect mixing ($\rho = 1$) for larger d/h. Usually, ρ was highest in the tails of the profiles, where θ_{rms} was small. This was attributed to strong, but rare, eddies that would advect (in the transverse direction) both thermal wakes far away from their sources. Minima in ρ were observed for transverse locations near y_{s_av}/h when wake flapping was prominent (i.e., for $y_{s\_av}/h = 0.5$ and 1.0). The minima in ρ drifted towards the wall as x/h increased. (This only occurred for $y_{s\_av}/h = 0.2$ and 0.5, given that symmetry about the channel centreline must hold when $y_{s\_av}/h = 1.0$.)

To facilitate the comparison of the correlation coefficient resulting from different combinations of source locations, ρ_{min} and $\rho_{ys\_av/h}$ were examined. The separation distance between the two line sources was a dominant factor in their evolutions; the closer the line sources were, the faster their thermal fields mixed. The effect of y_{s_av}/h was not as important, except when near the wall. Here, the high level of turbulence was found to accelerate the mixing, causing the correlation coefficient to increase rapidly.

For sources with $y_{s\_av}/h = 1.0$ (i.e., sources located in the least inhomogeneous region of the flow), ρ_{min} evolved in a similar manner to what has been observed in homogeneous, isotropic, grid-generated turbulence. Nevertheless, attempts to reduce the number of relevant parameters for ρ_{min}, as done in grid turbulence (Warhaft, 1984), were unsuccessful, thus demonstrating how the inhomogeneity of channel flow remains non-negligible.

The co-spectra followed the same trends as ρ, increasing with downstream distance. The coherency spectra, were relatively constant across all scales for $y_{s\_av}/h = 0.5$ and 1.0. However, for source combinations with $y_{s\_av}/h = 0.2$, the coherency evolved much more rapidly at the large scales than at the small ones.

5.1 Future work

The study of passive scalar mixing in turbulent flows can be extended in many directions. More specifically, with respect to the mixing of scalars in turbulent channel flow, the details of the scalar mixing process in the near-wall region (and its relation to the coherent structures therein) is not well understood. Additional research studying scalar dispersion in this region, from both single and multiple sources, would be of benefit. Furthermore, the present experiments have only studied the effect of the inhomogeneous nature of the flow on the dispersion on the transverse direction. The inhomogeneity presumably also effects the lateral dispersion. The latter could be studied by experiments using either i) line sources oriented in the wall-normal direction, or ii) point sources. The lateral dispersion could be measured at different wall-normal distances in such experiments.

From the results with $y_{s\_av}/h = 0.5$ and 1.0, where the inhomogeneity is weak, an approximate reduction of the number of dependent parameters in the central zone of the channel may be possible. Therefore, a deeper study of potential non-dimensionalization schemes could be a possible extension of this work. Another such extension could be the

study of the mixing from three or more line sources. Such experiments are feasible using the inference method and could be easily performed with the current apparatus.

Finally, the study of the mixing of non-passive scalars in turbulent flows would be of interest and significant relevance. For example, the extent to which the dispersion of a dense gas, like ammonia, differs from passive scalar dispersion in a bounded flow is unknown. Such information could be obtained through similar experiments.

Appendix

Given that the individual source locations in the present work were different than those employed in Lavertu & Mydlarski (2005), the single-line-source RMS profiles for the present experiments are described in this Appendix. (These data were used in the calculation of the nondimensional correlation coefficients in Chapter 4.) These data are provided to be able to infer the scalar covariances from then results of Chapter 4, if desired.

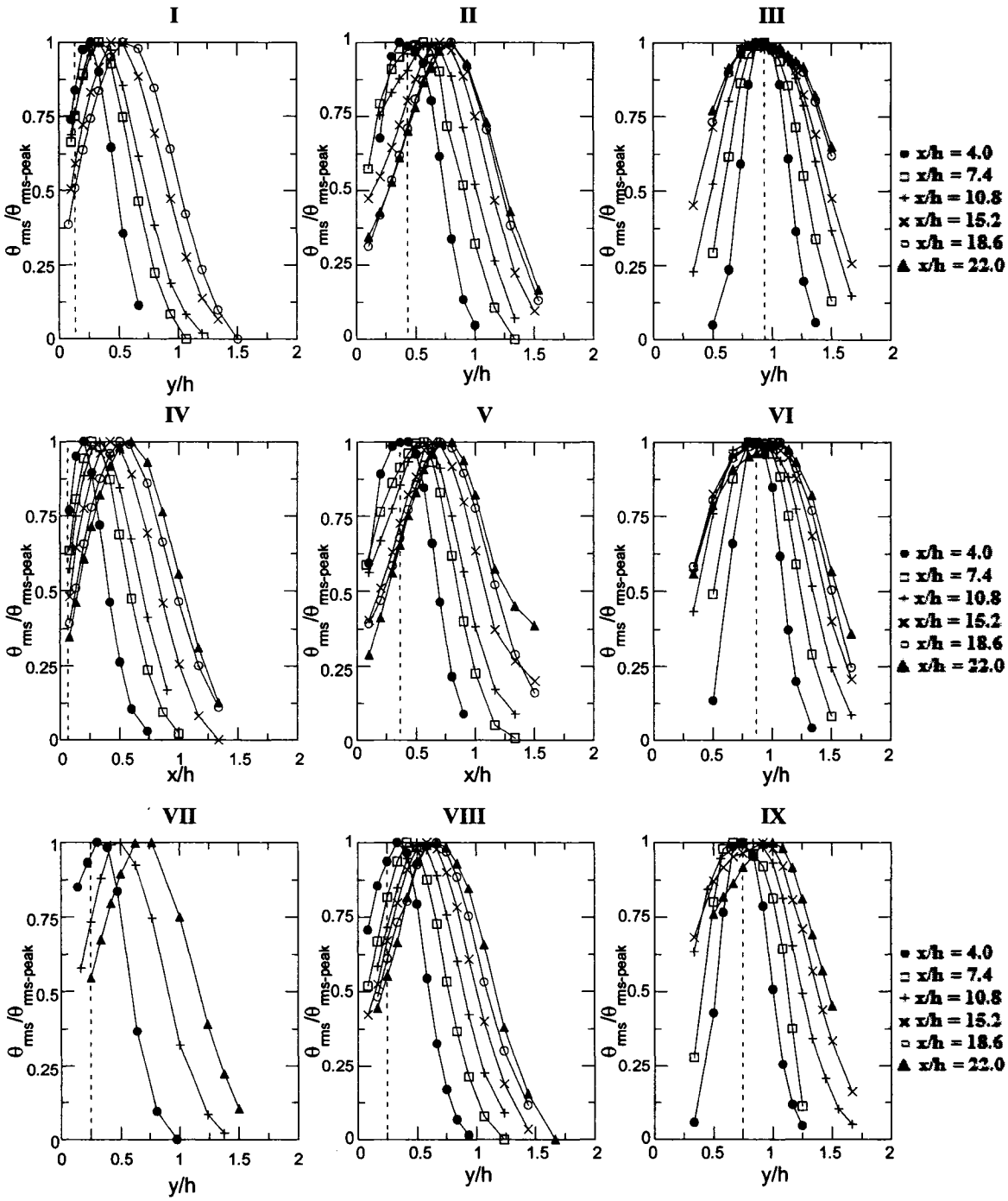

Figure A.1 Transverse normalized θ_{rms} profiles for 9 (closer) line source locations. The vertical lines are drawn at the location of the line source. Each location corresponds to the line closest to y/h = 0 in two line sources combination.

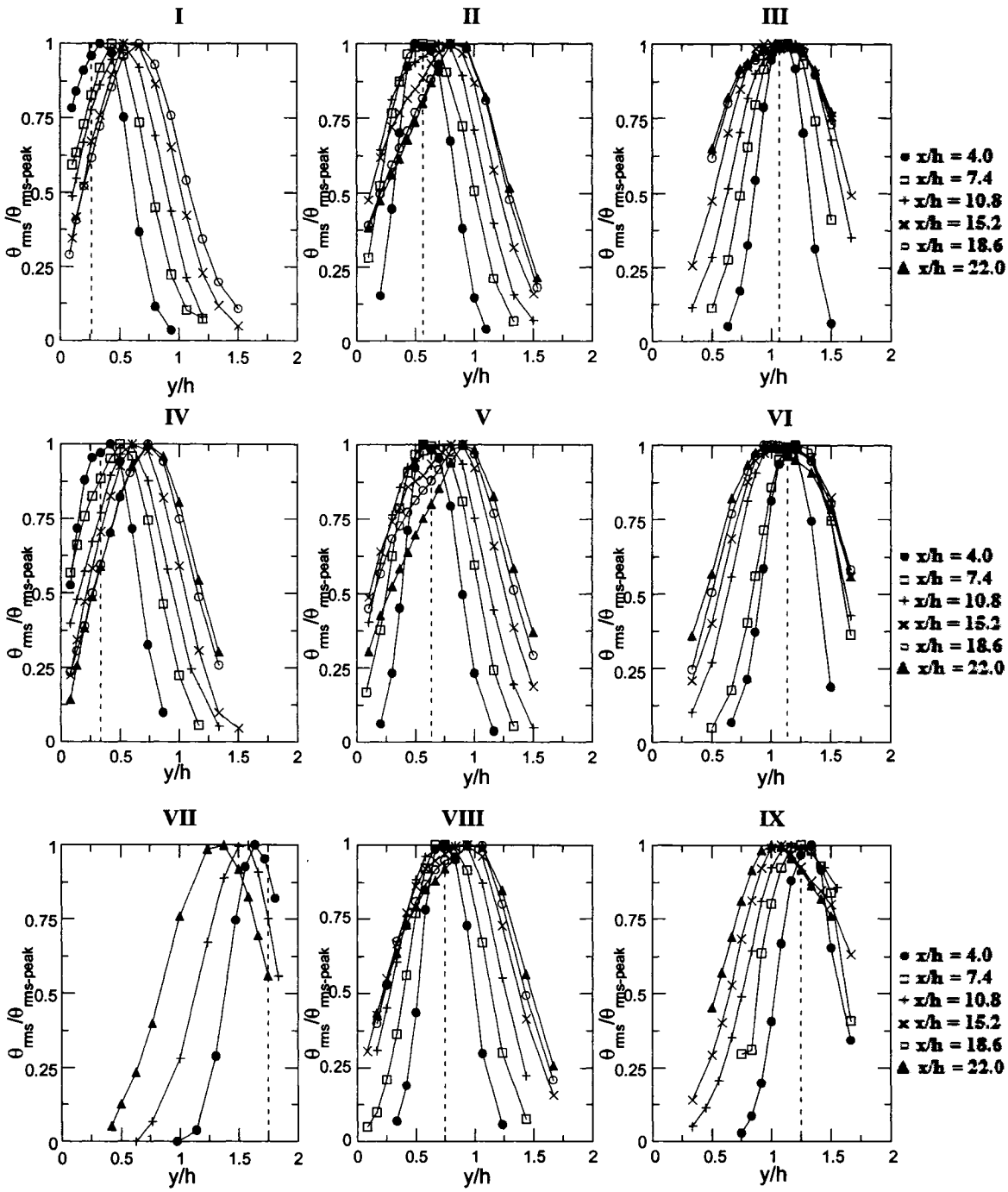

Figure A.2 Transverse normalized θ_{rms} profiles for 9 (farther) line source locations. The vertical lines are drawn at the location of the line source. Each location corresponds to the line farthest from y/h = 0 in a two line sources combination.

Bibliography

Adrian, R.J. 1996. Laser velocimetry. *Fluid Mechanics Measurements, Second Edition.* Taylor & Francis, 175-300.

Batchelor, G.K. 1953. *The Theory of Homogeneous Turbulence.* Cambridge University Press.

Baldyga, J. and Bourne, J.R. 1999. *Turbulent Mixing and Chemical Reactions.* Wiley.

Beaulac, S. and Mydlaski, L. 2004. Dependence on the initial conditions of scalar mixing in the turbulent wake of a circular cylinder. *Phys. Fluids* **16**, 3161-3172.

Bernard, P.S. and Rovelstad, A.L. 1994. On the physical accuracy of scalar transport modeling in inhomogeneous turbulence. *Phys. Fluids* **6**, 3093-3108.

Blevins, R.D. 1990. *Flow-Induced Vibrations, Second Edition.* Krieger.

Brethouwer, G., Boersma, B.J., Pourquié, M.B.J.M., Nieuwstadt, F.T.M. 1999. Direct numerical simulation of turbulent mixing of a passive scalar in pipe flow. *Eur. J. Mech. B/Fluids* **18**, 739-756.

Bruun, H.H. 1995. *Hot-Wire Anemometry.* Oxford University Press.

Buchhave, P., George, W.K. and Lumley J.L. 1979. The measurement of turbulence with the laser-doppler anemometer. *Annu. Rev. Fluid Mech.* **11**, 443-503.

Comte-Bellot, G. and Corrsin, S. 1966. The use of a contraction to improve the isotropy in grid-generated turbulence. *J. Fluid Mech.* **25**, 657-682.

Comte-Bellot, G. 1976. Hot-wire anemometry. *Annu. Rev. Fluid Mech.* **8**, 209-231.

Dinavahi, S.P.G., Breuer, K.S. and Sirovich, L. 1995. Universality of probability density functions in turbulent channel flow. *Phys. Fluids* **7** (5), 1122-1129.

El Kabiri, M., Paranthoën, P., Rosset, L. and Lecordier, J.C. 1998. Fluctuations de température et flux de chaleur en aval d'une source linéaire placée dans une couche limite turbulente. *Rev. Gén. Therm.* **37**, 181-194.

Grandmaison, E.W., Pollard, A. and NG, S. 1991. Scalar mixing in a free, turbulent rectangular jet. *Int. J. Heat Mass Transfer* **34**, 2653-2662.

Hinze, J.O. 1959. *Turbulence.* McGraw-Hill.

Iliopoulos, I. and Hanratty, T.J. 1999. Turbulent dispersion in a non-homogeneous field. *J. Fluid Mech.* **392**, 45-71.

Incropera, F.P., Kerby, J.S., Moffatt, D.F. and Ramadhyani, S. 1986. Convection heat transfer from discrete heat sources in a rectangular channel. *Int. J. Heat Mass Transfer* **29**, 1051-1058.

Jaberi, F.A., Colucci, P.J. 2003. Large eddy simulation of heat and mass transport in turbulent flows. Part 2: velocity field. *Int. J. Heat Mass Transfer* **46**, 1827-1840.

Karnik, U. and Tavoularis, S. 1989. Measurement of heat diffusion from a continuous line source in a uniformly sheared turbulent flow. *J. Fluid Mech.* **202**, 233-261.

Kim, J., Moin, P. and Moser, R. 1987. Turbulence statistics in fully-developed channel flow at low Reynolds number. *J. Fluid Mech.* **177**, 133-166.

Kolmogorov A.N. 1941. The local structure of turbulence in incompressible viscous fluid for very large Reynolds number. *Dokl. Akad. Nauk. SSSR* **30**, 9-13.

Kontomaris, K. and Harantty, T.J. 1994. Effect of a molecular diffusivity on point source diffusion in the center of a numerically simulated turbulent channel flow. *Int. J. Heat Mass Transfer* **37**, 1817-1828.

Lavertu, R. 2002. *Scalar Dispersion in Turbulent Channel Flow*. M. Eng. Thesis, McGill University.

Lavertu, R.A. and Mydlarski, L. 2005, Scalar mixing from a concentrated source in turbulent channel flow. *J. Fluid Mech.* **528**, 135-172.

Lemay, J. and Jean, Y. 2001. *Constant Current Anemometer Utilization Guide.* University Laval.

Lemay, J. and Benaïssa, A. 2001. Improvement of cold-wire response for measurement of temperature dissipation. *Exps. Fluids* **31**, 347-356.

Lesieur, M. 1997. *Turbulence in Fluids.* Kluwer Academic Publisher.

Lyons, S.L. and Hanratty, T.J. 1991. Direct numerical simulation of passive heat transfer in a turbulent channel flow. *Int. J. Heat Mass Transfer* **34**, 1149-1161.

Liu, Z., Adrian, R.J. and Hanratty, T.J. 2001. Large-scale modes of turbulent channel flow: transport and structure. *J. Fluid Mech.* **448**, 53-80.

Mehta, R.D. 1977. The aerodynamic design of blower tunnels with wide-angle diffusers. *Prog. Aerospace Science* **18**, 59-120.

McLeod, M.S. 2000. *On the Design and Testing of a High-aspect-ratio Channel for Turbulent Flow Measurements.* Honours thesis, McGill University.

Monin, A.S. and Yaglom, A.M. 1975. *Statistical Fluid Mechanics*. MIT Press.

Na, Y. and Harantty, T.J. 2000. Limiting behavior of turbulent scalar transport close to a wall. *Int. J. Heat Mass Transfer* **43**, 1749-1758.

Orlandi, P. and Leonardi, S. 2004. Passive scalar in a turbulent channel flow with wall velocity disturbances. *Flow Turb. Comb.* **72**, 181-197.

Papavassiliou, D.V. and Harantty, T.J. 1997. Transport of a passive scalar in a turbulent channel flow. *Int. J. Heat Mass Transfer* **40**, 1303-1311.

Paranthoën, P., Fouari, A., Dupont, A. and Lecordier, J.C. 1988. Dispersion measurements in turbulent flows. *Int. J. Heat Mass Transfer* **31**, 153-165.

Paranthoën, P. and Lecordier, J.C. 1996. Mesures de température dans les écoulements turbulents. *Rev. Gén. Therm.* **35**, 285-308.

Perry, A.E. 1982. *Hot-Wire Anemometry*. Clarendon Press.

Pope, S.B. 2000. *Turbulent Flows*, Cambridge University Press.

Poreh, M. and Cermak, J.E. 194. Study of diffusion from a line source in a turbulent boundary layer. *Int. J. Heat Mass Transfer* **7**, 1083-1095.

Poreh, M. and Hsu, K.S. 1971. Diffusion from a line source in a turbulent boundary layer. *Int. J. Heat Mass Transfer* **14**, 1473-1483.

Reshotko, E., Saric, W.S. and Nagib, H.M. 1997. Flow quality issues for large wind tunnels. *AIAA 35th Aerospace Sciences Meeting and Exhibit.*

Richardson, L.F. 1925 *Big Whirls.*

Shah, D.A., Chambers, A.J. and Antonia, R.A. 1983. Reynolds number dependence of a fully-developed turbulent duct flow. *Eighth Australian Fluid Mechanics Conference*, University of Newcastle.

Shlien, D.J. and Corrsin, S. 1976. Dispersion measurements in a turbulent boundary layer. *Int. J. Heat Mass Transfer* **19**, 285-295.

Shraiman, B.I. and Siggia, E.D. 2000. Scalar turbulence. *Nature* **405**, 639-646.

Stapountzis, H., Sawford, B.L., Hund, J.C.R. and Britter, R.E. 1986. Structure of the temperature field downwind of a line source in grid turbulence. *J. Fluid Mech.* **165**, 401-424.

Sreenivasan, K.R. 1991. On local isotropy of passive scalar in turbulent shear flows. *Proc. R. Soc. London. A* **434**, 165-182.

Tavoularis, S. and Corrsin, S. 1981. Experiments in nearly homogenous turbulent shear-flow with a uniform mean temperature gradient. *J. Fluid Mech.* **104**, 311-347.

Taylor G.I. 1935. Statistical theory of turbulence. IV-Diffusion in a turbulent air stream. *Proc. R. Soc. Lond. A* **151**, 465-478.

Tennekes, H. and Lumley, J.L. 1972. *A First Course in Turbulence*, MIT Press.

Tong, C. and Warhaft, Z. 1995. Passive scalar dispersion and mixing in a turbulent jet. *J. Fluid Mech.* **292**, 1-39.

Townsend, A.A. 1954. The diffusion behind a line source in homogeneous turbulence. *Proc. R. Soc. Lond. A* **224**, 487.

Townsend, A.A. 1976. The structure of turbulent shear flow. Cambridge University Press.

Uberoi, M.S. and Corrsin, S. 1952. Diffusion from a line source in isotropic turbulence. *NACA Tech. Note* **2710**.

Veeravalli, S. and Warhaft, Z. 1990. Thermal dispersion from a line source in the shearless turbulence mixing layer. *J. Fluid Mech.* **216**, 35-70.

Vinçont, J-Y., Simoëns, S., Ayrault, M. and Wallace, J.M. 2000. Passive scalar dispersion in a turbulent boundary layer from a line source at the wall and downstream of an obstacle. *J. Fluid Mech.* **424**, 127-167.

Vrieling, A.J. and Nieuwstadt, F.T.M. 2003. Turbulent dispersion from nearby point sources-interference of the concentration statistics. *Atmos. Environ.* **37**, 4493-4506.

Walker, D.A. 1987. A fluorescence technique for measurement of concentration in mixing liquids. *J Phys E: Sci Instrum* **20**, 217-224.

Warhaft, Z. 1981. The use of dual heat injection to infer scalar covariance decay in grid turbulence. *J. Fluid Mech.* **104**, 93-109.

Warhaft, Z. 1984. The interference of thermal fields from line sources in grid turbulence. *J. Fluid Mech.* **144**, 363-387.

Warhaft, Z. 2000. Passive scalars in turbulent flows. *Annu. Rev. Fluid Mech.* **32**, 203-240.

Wyngaard J.C. 1968. Measurement of small-scale turbulence structure with hot wires. *J. Sc. Intr. Series 2* **1**, 1105-1108.